

ИНСТИТУТ ЗА ФИЗИКУ

ПРИМЉЕНО: 30. 08. 2023			
Рад.јед.	Б р о ј	Арх.шифра	Прилог
0801	1234/1		

Научном већу Института за физику у Београду

Предмет:

Молба за покретање поступка за стицање звања истраживач сарадник

С обзиром на то да испуњавам услове предвиђене Правилником о стицању истраживачких и научних звања, прописаног од стране ресорног Министарства, молим Научно веће Института за физику у Београду да покрене поступак за мој избор у звање истраживач сарадник.

У прилогу достављам:

1. Мишљење руководиоца лабораторије са предлогом комисије за избор у звање;
2. Стручну биографију;
3. Преглед научних активности;
4. Списак научних радова;
5. Уверење о статусу студента докторских студија;
6. Копију диплома са основних и мастер студија;
7. Копије научних радова.

С поштовањем,

Марија Шиндик

истраживач приправник

Шиндик Марија



Број _____

Датум _____

ПРИМЉЕНО:			
Рад.јед.	б р о ј	Арх.шифра	Прилог
0801	1234/2		

Научном већу Института за физику у Београду

Предмет: Мишљење руководиоца лабораторије о избору Марије Шиндик у звање истраживач сарадник

Марија Шиндик је ангажована у Лабораторији за примену рачунара у науци, у оквиру Националног центра изузетних вредности за изучавање комплексних система Института за физику у Београду. У свом истраживачком раду бави се физиком ултрахладних диполних квантних гасова. С обзиром да испуњава све предвиђене услове у складу са Правилником о стицању истраживачких и научних звања, сагласан сам са покретањем поступка за избор Марије Шиндик у звање истраживач сарадник.

За састав комисије за избор Марије Шиндик у звање истраживач сарадник предлажем:

- (1) др Антун Балаж, научни саветник, Институт за физику у Београду,
- (2) др Ивана Васић, виши научни сарадник, Институт за физику у Београду,
- (3) др Светислав Мијатовић, доцент Физичког факултета Универзитета у Београду.

др Антун Балаж
научни саветник
руководилац Лабораторије за
примену рачунара у науци

Биографски подаци кандидаткиње

Марија Шиндик рођена је 03.01.1997. године у Београду, где је завршила основну школу и Математичку гимназију, као носилац Вукове дипломе. Током средње школе имала је запажен успех на такмичењима из физике на државном и интернационалном нивоу.

Школске 2015/16. године уписала је Физички факултет Универзитета у Београду, смер Теоријска и експериментална физика. Основне академске студије завршила је 2019. године са просечном оценом 10, и проглашена је студентом генерације на Физичком факултету.

Мастер академске студије је завршила 2020. године на истом смеру, такође са просечном оценом 10. Мастер рад под називом „Quantum Droplets in Dipolar Ring-shaped Bose-Einstein Condensates“ („Квантне капљице у диполним прстенастим Бозе-Ајнштајн кондензатима“), одбранила је 30.09.2020. године, под руководством др Антуна Балажа.

Школске 2020/21. године је уписала докторске студије на Физичком факултету у Београду, ужа научна област физика кондензоване материје и статистичка физика. Након завршене прве године, школске 2021/22. уписала је докторске студије на Универзитету у Тренту у Италији, у Питаевски центру за Бозе-Ајнштајн кондензацију, под менторством Alessio Recati-ја. Главна тема изучавања је суперсолидно стање у ултрахладним диполним Бозе гасовима.

Током основних и мастер студија била је ангажована на семинару физике у Истраживачкој станици Петница, од 2016. до 2018. године као сарадник, а 2019. и 2020. године као руководилац семинара. Од 2015. до 2020. године је била ангажована у Математичкој гимназији као асистент у додатној настави, и школске 2020/21. као наставник физике.

Током основних студија била је на студентским праксама на Институту за физику у Београду и у Институту DESY у Хамбургу. Као резултат ових пракси, објавила је два рада у часописима категорија M21 и M22. Током докторских студија објавила је један научни рад у часопису категорије M21, и један који је у фази рецензије. Имала је неколико доприноса са међународних скупова (катеорије M34).

Преглед научне активности кандидаткиње

Марија Шиндик се у досадашњем раду бавила нумеричким изучавањем диполних ултрахладних Бозе гасова, односно система атома са јаким перманентним магнетним диполним моментом, на ниским температурама на којима долази до Бозе-Ајштајн кондензације. Посебан акценат је стављен на суперсолидна стања, за која је недавно показано да је постоје у овим системима у одређеном опсегу параметара. Ово интригантно стање материје је карактерисано спонтаним и истовременим нарушењем фазне и трансляционе симетрије, резултирајући у неинтуитивној коегзистенцији суперфлуидних и кристалних особина.

Једна од фундаменталних карактеристика суперфлуидности је постојање квантизованих вортекса. Иако постоје скорашња нумеричка истраживања која показују њихово постојање и у суперсолидној фази, њихова експериментална детекција и даље представља изазов. Разлог је што се језгра вортекса у суперсолидној фази налазе на местима између квантних капљица, која су и без присуства вортекса карактерисана малом густином. Стога је детекција конвенционалним методама снимања густине таласне функције након експанзије, и повезивања „рупа“ у густини са вортексима, у овом случају јако тешко.

Један део истраживања кандидаткиње се бавио конструкцијом протокола нуклеације и детекције вортекса у диполним Бозе гасовима у хармонијској замци. Метод је базиран на мењању дужине расејања система контролом спољашњег магнетног поља, што доводи до фазног прелаза између суперфлуидне и суперсолидне фазе. Почевши од споро ротирајуће конфигурације у суперфлуидној фази која не поседује вортекс, прелазак у суперсолидну фазу доводи до нуклеације вортекса, због значајно смањене критичне угаоне фреквенције у овој фази. Након што је вортекс креиран, показано је да остаје стабилан при поновном преласку фазног прелазу у суперфлуидно стање, где је његова експериментална детекција могућа. Ови резултати могу имати значајан утицај на тренутне експерименте, пружајући метод провере суперфлуидног карактера диполних суперсолидних стања.

Још једна значајна карактеристика суперсолидне фазе је постојање Голдстонових мода, као последица спонтаног нарушења фазне и трансляционе симетрије. У другом делу истраживања кандидаткиње, систем који се посматра је у спољашњем потенцијалу прстенастог облика, где долази до појаве две Голдстонове моде. Оне се побуђују тако што се нагло уклони периодична пертурбација пропорционална са $\cos \theta$, где је θ азимутални угао. Анализирањем резултујућих осцилација гаса, могуће је одредити вредности две брзине звука које су повезане са две Голдстонове моде. Ове вредности су анализирани коришћењем хидродинамичке теорије суперсолидног стања на апсолутној нули. Овај приступ омогућава одређивање модула компресибилности слојева, као и суперфлуидне фракције, која се подудара са Leggett-овом проценом неklasичног момента инерције. Ово истраживање пружа оквир за експериментално одређивање релевантних параметара хидродинамичке теорије суперсолидног стања.

Списак објављених радова кандидаткиње

Радови објављени у научним часописима међународног значаја

- [1] M. Šindik, T. Zavišlak, A. Recati, and S. Stringari, *Sound, superfluidity and layer compressibility in a ring dipolar supersolid*, arXiv:2308.05981v1 (2023). [in the review process]
- [2] M. Šindik, A. Recati, S. M. Roccuzzo, L. Santos, and S. Stringari, *Creation and robustness of quantized vortices in a dipolar supersolid when crossing the superfluid-to-supersolid transition*, *Phys. Rev. A* **106**, L061303 (2022). [M21]
- [3] E. Zapolnova, R. Pan, T. Golz, M. Šindik, M. Nikolic, M. Temme, M. Rabasovic, D. Grujic, Z. Chen, S. Toleikis and N. Stojanovic, *XUV-driven plasma switch for THz: new spatiotemporal overlap tool for XUV–THz pump–probe experiments at FELs*, *J. Synchrotron Rad.* **27**, 11 (2020). [M22]
- [4] M. Šindik, A. Sugita, M. Šuvakov, V. Dmitrašinović, *Periodic three-body orbits in the Coulomb potential*, *Phys. Rev. E* **98**, 060101(R) (2018). [M21]

Саопштења са међународних скупова штампано у изводу (категирија М34)

- [1] M. Šindik, A. Recati, S. M. Roccuzzo, L. Santos, and S. Stringari: “Quantized vortices in dipolar BECs when crossing the superfluid supersolid phase transition”; Photonica 2023; Belgrade, Serbia; 28 Aug–1 Sept 2023
- [2] M. Šindik, A. Recati, S. M. Roccuzzo, L. Santos, and S. Stringari: “Creation and robustness of quantized vortices in a dipolar supersolid when crossing the superfluid-to-supersolid transition”; Ultracold Quantum Matter: Basic Research and Applications; Bad Honnef, Germany; 12-16 Dec 2022
- [3] M. Šindik, A. Recati, S. M. Roccuzzo, L. Santos, and S. Stringari: “Creation and robustness of quantized vortices in a dipolar supersolid when crossing the superfluid-to-supersolid transition”; EMMI Workshop on Long-Range Ultracold Interactions 2022; Innsbruck, Austria; 6-9 Sept 2022
- [4] M. Šindik, A. Pelster, and A. Balaž: “Quantum Droplets in Dipolar Ring-shaped Bose-Einstein Condensates”; Photonica 2021; Belgrade, Serbia; 23-27 Aug 2021
- [5] M. Šindik, A. Pelster, and A. Balaž: “Quantum Droplets in Dipolar Ring-shaped Bose-Einstein Condensates”; Exploring Quantum Many-Body Physics with Ultracold Atoms and Molecules; Bad Honnef, Germany (Online); 14-18 Dec 2020



UNIVERSITÀ
DI TRENTO

20222808535/2022

Student ID number: 231788

We hereby certify that **SINDIK MARIJA** born in BELGRADE - SERBIA - on 3rd January 1997, is enrolled in the second year of the Doctoral Programme in *Physics*, 37th cycle, with administrative seat at the University of Trento (Italy).

We also certify that **SINDIK MARIJA** receives a doctoral grant from the University of Trento and a 50% increase of the scholarship for research period spent abroad, as foreseen by the University Regulation for Doctoral Programmes.

The Doctoral Programme in *Physics* lasts three years (the 37th cycle from 01/11/2021 to 31/10/2024).

The present certificate is issued on unstamped paper for the use foreseen by law. For different use a revenue stamp is to be applied.

TRENTO, 22/08/2023

Head of Division
Dott.ssa Paola Fusi
PhD Office
Science and Technology Area



UNIVERSITÀ
DI TRENTO
Education and
student services management

The above information is extracted from the University of Trento database. For official purposes this certificate has to be produced in Italian and English version. Signature is omitted in accordance with Decree Law 12/02/1993, n. 39. This certificate may not be issued, or otherwise made available, to any public administration or private organizations operating in the public services (in accordance with article 40 of Italian Law no. 445/2000).



Република Србија
Универзитет у Београду

Оснивач: Република Србија

Дозволу за рад број 612-00-02666/2010-04 од 12. октобра 2011.
године је издало Министарство просвете и науке Републике Србије

Физички факултет, Београд

Оснивач: Република Србија

Дозволу за рад број 612-00-02409/2014-04 од 8. септембра 2014. године је издало
Министарство просвете, науке и технолошког развоја Републике Србије



УБ

Диплома

Марија, Никола, Шиндик

рођена 3. јануара 1997. године, Београд, Република Србија, уписана школске 2015/2016.

године, а дана 30. септембра 2019. године завршила је основне академске студије,
првог степена, на студијском програму Теоријска и експериментална физика, обима
240 (двеста четрдесет) бодова ЕСПБ са просечном оценом 10,00 (десет и 0/100).

На основу тога издаје јој се ова диплома о стицању високог образовања и стручном називу

дипломирани физичар

Број: 11280700

У Београду, 29. октобра 2020. године

Декан
Проф. др Иван Бецца

Ректор
Проф. др Иванка Појовић

00112927



Република Србија
Универзитет у Београду

Оснивач: Република Србија

Дозволу за рад број 612-00-02666/2010-04 од 12. октобра 2011. године је издало Министарство просвете и науке Републике Србије



УБ

Физички факултет, Београд

Оснивач: Република Србија

Дозволу за рад број 612-00-02409/2014-04 од 8. септембра 2014. године је издало Министарство просвете, науке и технолошког развоја Републике Србије

Диплома

Марија, Никола, Шиндик

рођена 3. јануара 1997. године, Београд, Република Србија, уписана школске 2019/2020.

године, а дана 30. септембра 2020. године завршила је мастер академске студије,

другог степена, на студијском програму Теоријска и експериментална физика,

обима 60 (шездесет) бодова ЕСПБ са просечном оценом 10,00 (десет и 0/100).

На основу тога издаје јој се ова диплома о стеченом високом образовању и академском називу

мастер физичар

Број: 11279200

У Београду, 29. октобра 2020. године

Декан
Проф. др Иван Белча

Ректор
Проф. др Иванка Појовић

00112942

Sound, superfluidity and layer compressibility in a ring dipolar supersolid

Marija Šindik,^{1,*} Tomasz Zawiślak,^{1,*} Alessio Recati,^{1,†} and Sandro Stringari¹

¹*Pitaevskii BEC Center, CNR-INO and Dipartimento di Fisica,
Università di Trento, Via Sommarive 14, 38123 Povo, Trento, Italy*

We propose a protocol to excite the Goldstone modes of a supersolid dipolar Bose-Einstein condensed gas confined in a ring geometry. By abruptly removing an applied periodic modulation proportional to $\cos(\varphi)$, where φ is the azimuthal angle, we explore the resulting oscillations of the gas, by solving the extended Gross-Pitaevskii equation. The value of the two longitudinal sound velocities exhibited in the supersolid phase are analyzed using the hydrodynamic theory of supersolids at zero temperature. This approach allows for the determination of the layer compressibility modulus as well as of the superfluid fraction f_S , in agreement with the Leggett estimate of the non-classical moment of inertia.

A key consequence of the spontaneous breaking of continuous symmetries is the occurrence of Goldstone modes, which, in the presence of finite range interactions, take the form of gapless excitations in the long wavelength limit. The identification and the experimental observation of the Goldstone modes then represents a question of central interest in various fields of science, including elementary particle physics, magnetism, superfluidity and superconductivity. The recent realization of supersolidity has raised the question of the identification of the corresponding Goldstone modes which are the consequence of the spontaneous and simultaneous breaking of phase symmetry and translational invariance, ensuring the non intuitive co-existence of superfluid and crystal features. From the theoretical side the study of the Goldstone modes in supersolids has an old history, starting from the pioneering work of Andreev and Lifshitz [1] (see also [2, 3]), and more recent papers based on numerical simulations on atomic Bose gases interacting with soft-core potentials [4–6], spin orbit coupled gases (see the recent reviews [7, 8] and reference therein) and dipolar gases [9] (see also the recent Perspective [10] and references therein). First experimental evidence for the occurrence of Goldstone modes in a supersolid has been recently reported in the case of a dipolar gas confined in a harmonic trap, where the modes take the form of discretized oscillations and in particular with the emergence of novel crystal-like oscillations as soon as one enters the supersolid phase [11–13]. The use of harmonic trapping potentials, inducing the non-homogeneity of the gas, together with a relatively small number of droplets which form the non-superfluid component of the gas within the supersolid/crystal phase, limits the possibility to fully appreciate the rich dynamics of the dipolar gas as a bulk supersolid. For cold gases with short range interaction one can use box potentials to avoid or strongly reduce the inhomogeneity. However, when the dipolar interaction dominates the physics of the gas, such an approach does not work due to strong edge effect [14].

In this Letter we propose to use a ring potential and to measure the response to a periodic static perturbation in order to extract the low momenta dispersion relation

of the system. The calculated sound velocities are then analyzed employing the hydrodynamic theory of supersolids. In particular, we determine the layer compressibility modulus and the superfluid fraction, pointing out their role in the propagation of sound in the supersolid phase. Interestingly, ring traps offer one of the simplest realizations of matter wave circuits, with important perspectives in the emerging field of atomtronics [15, 16].

The model and its quantum phases. In a dilute dipolar Bose gas, the atoms interact by a delta-contact potential $V_c(\mathbf{r}) = g\delta(\mathbf{r})$, with the coupling constant $g = 4\pi\hbar^2 a/m > 0$ fixed by the atomic mass m and the s-wave scattering length a ; and by the dipolar potential $V_{dd}(\mathbf{r}) = \frac{\mu_0\mu^2}{4\pi} \frac{1-3\cos^2\theta}{|\mathbf{r}|^3}$ with θ the angle between \mathbf{r} and the direction z of the externally applied magnetic field, which aligns the atomic magnetic dipole moments μ . The most important parameter to determine the zero temperature phase diagram of the gas is the ratio between the strengths of the contact and the dipolar interactions, $\epsilon_{dd} = a_{dd}/a$ with $a_{dd} = \mu_0\mu^2/12\pi\hbar^2$ the so-called dipolar length. For small enough ϵ_{dd} the system forms a Bose-Einstein condensate (BEC), while by increasing it beyond a certain threshold, in three-dimensional uniform configurations, the system collapses due to the attractive nature of the dipolar interaction. Confining the gas along the z direction prevents this collapse, and three distinct phases occur: (i) a homogeneous BEC (superfluid phase), (ii) a supersolid phase in a very small interval of ϵ_{dd} , and (iii) a droplet crystal phase, i.e., independent droplets arranged in a crystal structure. In the present Letter we consider moreover that the gas is confined in the $x-y$ plane by a ring-shaped potential $V_{\text{ext}}(r_{\perp}, z) = m [\omega_{\perp}^2 (r_{\perp} - R)^2 + \omega_z^2 z^2] / 2$ with $r_{\perp} = \sqrt{x^2 + y^2}$, of radius $R = 7.64 \mu\text{m}$ and trap frequencies $\omega_z = \omega_{\perp} = 2\pi \cdot 100$ Hz, leading to the three phases reported in Fig. 2, calculated for $N = 80000$ ¹⁶⁴Dy atoms, corresponding to $a_{dd} = 132a_0$, where a_0 is the Bohr radius. We obtain a ring-shaped cloud of length $L \approx 49 \mu\text{m}$ [17] and width FWHM_{XY} changing from $1.41 \mu\text{m}$ in the superfluid to $0.7 \mu\text{m}$ approaching the crystal phase (see Fig.2). Due to magnetostriction, the cloud

is elongated in the third direction with $\text{FWHM}_Z \approx 4 \mu\text{m}$. The system is numerically studied within the so-called extended Gross-Pitaevskii equation [18] which in the last few years has been systematically employed to describe the equilibrium and dynamic properties of dipolar supersolids, in reasonably good agreement with the experimental findings.

The protocol. We first determine the state of the gas by applying a small static perturbation of the form $V_0 \cos \varphi$, where φ is the azimuthal angle along the ring, which produces stationary density modulations. We then suddenly set $V_0 = 0$, resulting in the excitation of the longitudinal phonon modes propagating along the ring. Similar protocols have been already applied to investigate the Doppler effect due to the presence of quantized vortices in a ring [19] and, more recently, to investigate the effect of superfluidity on the propagation of sound in a dilute Bose gas confined in a box in the presence of an external periodic potential [20].

An easy analysis of the response of the system can be obtained considering sufficiently large ring sizes for which the ring can be mapped in a linear tube configuration with imposed periodic boundary conditions. In particular we assume that the length L of the ring is much larger than its width, so that one can safely identify $\cos(\varphi)$ with $\cos(qx)$, where $q = 2\pi/L$ is the wave vector of the longitudinal excitation and the variable x , with $0 \leq x \leq L$, is the longitudinal coordinate along the tube. According to linear response theory, the quantity $\delta F = \langle \cos \varphi(t) \rangle - \langle \cos \varphi \rangle$, where the bar stays for the time average, should show, in the supersolid phase, a beating of two modes (see inset in Fig. 3)

$$\delta F(t) = V_0 \sum_{i=1,2} \chi_i(q) \cos(\omega_i(q)t) \quad (1)$$

with $\omega_i(q)$ approaching, for sufficiently small q (and hence large L), the linear phonon dispersion $\omega_i(q) \simeq c_i q$, with c_1 and c_2 hereafter called first and second sound velocities, respectively. The quantities $\chi_i(q)$, $i = 1, 2$, define the contributions of the two modes to the static response and hence to the compressibility sum rule according to

$$\chi(q) = \chi_1(q) + \chi_2(q) = \int_0^\infty d\omega \frac{S(q, \omega)}{\omega} \underset{q \rightarrow 0}{=} N\kappa \quad (2)$$

with κ the compressibility of the system (hereafter we set $\hbar = m = 1$, with m the atomic mass), while $S(q, \omega)$ is the dynamic structure factor. From the analysis of the measurable signal $\delta F(t)$ of Eq. (1) one can then determine the sound velocities c_1 and c_2 , and the relative contribution

$$R \equiv \frac{\chi^{(2)}}{\chi} = \frac{c_1^2 - c_\kappa^2}{c_1^2 - c_2^2} \quad (3)$$

of the lowest (second sound) mode to the compressibility sum rule, where we have defined $c_\kappa = \sqrt{\kappa^{-1}}$. Analogously,

the contribution of second sound to the f sum rule $m_1 = \int_0^\infty d\omega S(q, \omega)\omega = Nq^2/2$ is given by

$$\frac{m_1^{(2)}}{m_1} = \frac{c_2^2 c_1^2 - c_\kappa^2}{c_\kappa^2 c_1^2 - c_2^2}. \quad (4)$$

Hydrodynamic model for supersolidity. The speeds of sound obtained employing the protocol previously described can be used to extract important parameters characterising the system. For this purpose it is convenient to use the hydrodynamic theory of supersolids recently elaborated by Hofmann and Zwerger [3], inspired by the works of Andreev and Lifshitz [1] and Yoo and Dorsey [2]. This formulation, applicable to Galilean invariant systems, is particularly suitable to investigate the behavior of longitudinal phonons in the presence of a layer structure. This is reasonably well realized in highly elongated configurations of a dipolar supersolid, where the droplets effectively play the role of the layers. Neglecting the effects of the strain density coupling included in the general formulation of supersolid hydrodynamics [2], the approach, in this minimal hydrodynamic formulation, provides the following expression for the two sound velocities [3]

$$c_{1,2}^2 = \frac{c_\kappa^2}{2} \left[1 + \beta\kappa \pm \sqrt{(1 + \beta\kappa)^2 - 4f_S\beta\kappa} \right] \quad (5)$$

which depends on three fundamental parameters: the velocity c_κ , fixed by the compressibility parameter κ , the renormalized layer compressibility modulus $\beta = B/\rho_n$, given by the layer compressibility modulus B [21] divided by the normal density $\rho_n = \bar{\rho} - \rho_s$, and the superfluid fraction $f_S = \rho_s/\bar{\rho}$, with $\bar{\rho}$ the average 1D density. The relevant parameters $\beta\kappa$ and f_S can be expressed in terms of the first and second sound velocities according to the relations $\beta\kappa = (c_1^2 + c_2^2)/c_\kappa^2 - 1$ and $f_S\beta\kappa = c_1^2 c_2^2 / c_\kappa^4$, which directly follow from Eq. (5).

Let us now discuss the consequences of the hydrodynamic model in different phases of dipolar Bose gases:

(i) Superfluid phase ($f_S = 1$ and $\beta = 0$). Only the upper solution (first sound) of Eq. (5) is relevant and $c_1 = c_\kappa$.

(ii) Supersolid phase ($0 < f_S < 1$ and $\beta \neq 0$). In this most interesting case the deviations of the sound speeds from c_κ are determined by the dimensionless combination $\beta\kappa$ and by the superfluid fraction f_S . In particular, near the transition to the crystal phase, where the superfluid fraction is expected to vanish, the sound velocities approach the values

$$c_1 \rightarrow \sqrt{1 + \beta\kappa - \frac{f_S\beta\kappa}{1 + \beta\kappa}} c_\kappa, \quad c_2 \rightarrow \sqrt{f_S \frac{\beta\kappa}{1 + \beta\kappa}} c_\kappa \quad (6)$$

while the ratio R given by Eq. (3) approaches the value $\beta\kappa/(1 + \beta\kappa)$. It is worth noticing the close analogy between Eq. (6) and the dependence of the second sound

velocity on the superfluid density predicted by Landau's two-fluid hydrodynamic theory at finite temperature [22] (see also [23]).

It is also interesting to note that when the combination $\beta\kappa$ becomes very large the second sound velocity takes the form $c_2 = \sqrt{f_S}c_\kappa$ in the whole supersolid phase, it exhausts the compressibility sum rule, while its relative contribution to the f -sum rule (see Eq. (4)) exactly coincides with the superfluid fraction f_S . These results are consistent with the behavior of a superfluid in the presence of an optical lattice, where translational invariance is not broken spontaneously and the upper mode $\omega = c_1q$ is replaced by a gapped excitation. This case has been recently explored theoretically and experimentally in [20].

(iii) Crystal phase ($f_s = 0$ and $\beta \neq 0$). Only the upper solution survives in this case and the sound velocity takes the simple expression $c_1 = c_\kappa\sqrt{1 + \beta\kappa}$. Notice however that, differently from what happens in the superfluid phase, the first sound mode, while exhausting the f -sum rule, does not exhaust the compressibility sum rule, revealing the occurrence of a diffusive mode at zero frequency. Such a mode represents the natural continuation of the second sound mode beyond the transition to the crystal phase [24] and corresponds to the diffusive permeation mode of a smectic-A liquid crystal [3, 24]. The evolution of the second mode from a propagating to a diffusive one, is analogous to the fate of second sound in a uniform fluid above the superfluid critical temperature (see, e.g., [25, 26]).

Results. The compressibility κ of the gas can be extracted from the knowledge of the density changes caused by the static perturbation $V_0 \cos(\varphi)$ according to linear response theory (see Eq. (2)). Another option, which would not require the actual knowledge of V_0 , is to measure the relative contribution R (see Eq. (3)) of the second sound mode to the compressibility sum rule through the weights of the beating signal of Eq. (1).

Our protocol actually measures the static response function $\chi(q)/N$ (see Eqs. (1-2)) which coincides with the compressibility κ only in the long-wavelength limit $q \rightarrow 0$. Due to the finite size of the ring, the lowest accessible value is $q = 2\pi/L$, and it is consequently important to control the difference between $\chi(q = 2\pi/L)/N$ and the compressibility parameter $\kappa = (\bar{\rho} \partial\mu/\partial\bar{\rho})^{-1}$, where μ is the chemical potential. In our case the difference turns out to be about 15% in the superfluid phase and up to 30% close to the crystal phase. For consistency, we have used the values of κ given by the "measured" values $\chi(q = 2\pi/L)$. On the other hand, we verified that the superfluid fraction f_S , obtained by applying the hydrodynamic model to the results of the extended Gross-Pitaevskii simulation employing our protocol, is much less sensitive to finite size effects.

To illustrate the potential of the proposed protocol, in Fig. 1 we report the dispersion for larger values of q , within the superfluid phase, obtained by applying a

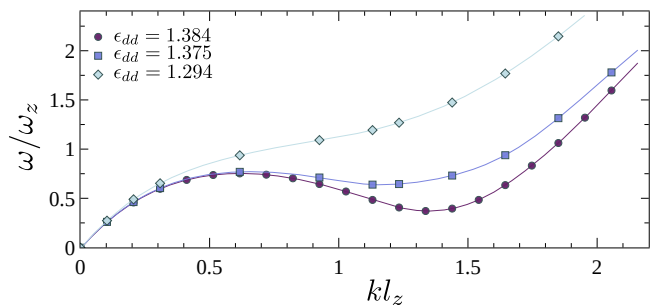


FIG. 1. Dispersion relation obtained using the proposed protocol, for three values of ϵ_{dd} approaching the superfluid-supersolid phase transition. The roton minimum softens near $k = \sqrt{2}/l_z$, where $l_z = \sqrt{\hbar/m\omega_z}$ is the harmonic oscillator length along the confined direction [27].

perturbation proportional to $\cos(n\varphi)$ with $n = 1, 2, \dots$, giving access to the phonon-maxon-roton dispersion, for which experimental evidence was reported in a superfluid dipolar gas using Bragg spectroscopy [28]. The figure clearly shows that the roton minimum becomes more pronounced as one approaches the transition to the supersolid phase, which in our configuration occurs for $\epsilon_{dd} = 1.387$.

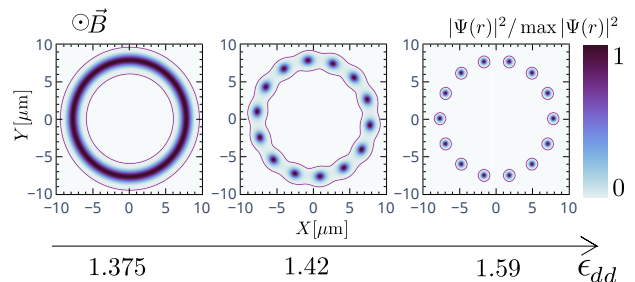


FIG. 2. Density plots of $N = 80000$ ^{164}Dy atoms in the superfluid, supersolid and crystal phase (left, middle, and right panel respectively), integrated over the z -axis, along which the magnetic field \vec{B} is aligned. Red contours mark 1% of the relative density $|\Psi(\mathbf{r})|^2 / \max |\Psi(\mathbf{r})|^2$.

In Fig. 2 we show the density profiles in the ring geometry calculated in the superfluid, supersolid and crystal phases [29]. In our simulations, based on the extended Gross-Pitaevskii equation, we have considered configurations with the same number of droplets (equal to 14) in both the supersolid and crystal phases. Actually, exact energy minimization would predict a decrease of the number of droplets when one approaches the transition to the crystal phase, leading to the small discontinuities in the resulting values of the observed quantities, which do not however affect the main conclusions of our work. The pinning of the number (and position) of droplets can be achieved by introducing a small additional periodic potential during the initial stage of the supersolid state

preparation. During the time evolution, once the periodic potential is removed, we observe that the number of droplets remains constant.

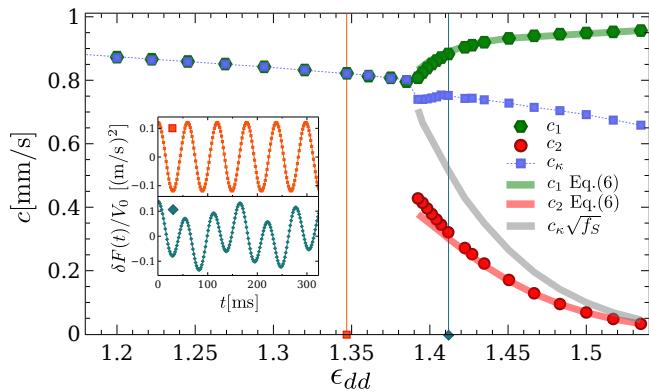


FIG. 3. Sound velocities c_1 and c_2 determined with the protocol (green hexagons and red circles respectively) across the superfluid-supersolid phase transition. The blue squares correspond to c_κ ($q = \frac{2\pi}{L}$). Both sound speeds are well captured by Eq. (6) (green and red solid lines) even far from the crystal phase. For completeness we also report the values $\sqrt{f_S}c_\kappa$ (gray solid line) found for an incompressible lattice (see text). The inset presents the time evolution of δF for two values of ϵ_{dd} marked with solid lines of corresponding colors. The data points are fitted with one (two) cosines in the superfluid (supersolid) phase with excellent quality.

Figs. 3 and 4 report the main results of our work, based on the combined application of the protocol and of the hydrodynamic model of supersolids. In Fig. 3 we show the calculated first and second sound velocities as a function of ϵ_{dd} , together with the value of c_κ , which coincides with the sound velocity in the superfluid phase. The figure clearly reveals the decrease of the second sound velocity as one approaches the transition to the crystal phase. We include also the lowest order expressions for the two sound speeds when $f_s \rightarrow 0$, Eq. (6) (red and green continuous lines), which are seen to be in good agreement with the calculated values also when the superfluid density is not that small. For comparison we also show the prediction $c_2 = \sqrt{f_S}c_\kappa$ (grey continuous line) which would hold in the presence of an optical lattice ($B \rightarrow \infty$) and which badly reproduces the actual values of c_2 in the supersolid phase. In Fig. 4a we report the results for the relevant parameter $\beta\kappa$ of the hydrodynamic model and the ratio R . An interesting outcome of our analysis is that while the speeds of sound, the compressibility and the dimensionless parameter $\beta\kappa$ show a jump at the superfluid-supersolid transition, the contribution of second sound to the compressibility sum rule, R , goes smoothly to zero. The same continuous vanishing is observed for the layer compressibility modulus B , as shown in Fig. 4b.

Moment of inertia and superfluid fraction. In the same Fig. 4c the results for the superfluid fraction, pre-

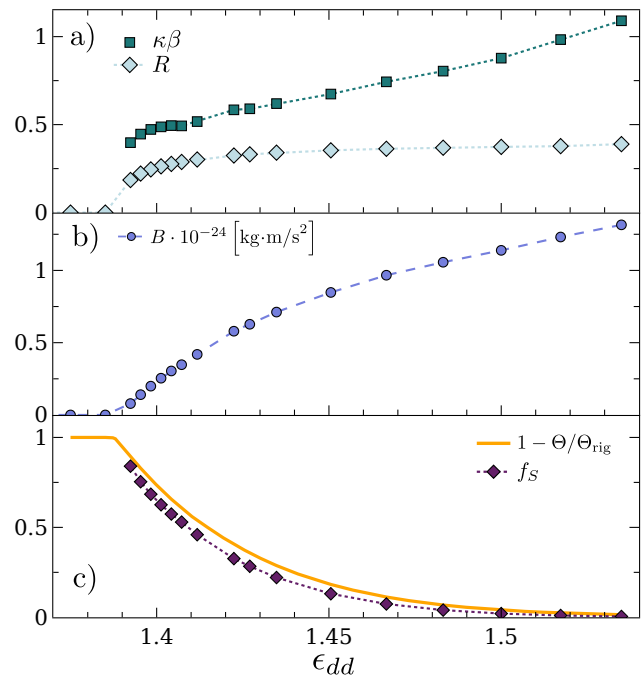


FIG. 4. Panel a) displays dimensionless parameters $\kappa\beta$ calculated using the hydrodynamic model (green squares), and the ratio $R = \chi^{(2)}/\chi$ (light blue diamonds) extracted from the time evolution of Eq. (1). In panel b) we show the emergence of finite layer compressibility modulus B . In panel c) we compare the extracted value of superfluid fraction f_s (purple diamonds) using the hydrodynamic relations Eq. (5), with the value determined via the non classical fraction of moment of inertia Eq. (7) (orange line).

dicted by the analysis of the sound velocities in the supersolid phase, are compared with the non classical fraction of the moment of inertia. In our narrow ring configuration the latter is expected to essentially coincide with the superfluid fraction, i.e.,

$$f_s \simeq 1 - \frac{\Theta}{\Theta_{rig}} \quad (7)$$

The moments of inertia in Eq. (7) are calculated in the ring geometry using the extended Gross-Pitaevskii equation. The moment of inertia Θ is fixed by the value $\langle J_z \rangle$ of the angular momentum induced by a rotational constraint of the form $-\Omega J_z$, according to the relationship $\Theta = \lim_{\Omega \rightarrow 0} \langle J_z \rangle / \Omega$, while $\Theta_{rig} = N \langle x^2 + y^2 \rangle$ is the classical rigid value [30]. We also verified that f_s from Eq. (7) practically coincides with the rigorous Leggett's upper bound $2\pi [\bar{\rho} \int_0^{2\pi} d\varphi / \rho(\varphi)]^{-1} \geq f_s$, where $\rho(\varphi)$ is the transverse integrated density along the ring [31]. The good agreement shown in Fig. 4c reveals the consistency of the extended Gross-Pitaevskii theory with the hydrodynamic model of the smectic superfluid phase developed in [3].

In conclusion, we have suggested a protocol to determine the Goldstone modes of a supersolid dipolar gas

confined in a ring and a way to identify the relevant parameters of the hydrodynamic theory of supersolids. Our work in particular paves the way for an experimental determination of the layer compressibility modulus and of the superfluid fraction, based on the measurement of the sound velocities.

Acknowledgement. We are grateful to Wilhelm Zwerger for many illuminating comments concerning the hydrodynamic model for supersolids when applied to configurations with density modulation along a single direction. Stimulating discussions with Giovanni Modugno and William Phillips are also acknowledged. We acknowledge support from the Provincia Autonoma di Trento, the Q@TN (the joint lab between University of Trento, FBK-Fondazione Bruno Kessler, INFN-National Institute for Nuclear Physics and CNR-National Research Council), the Italian MIUR under the PRIN2017 project CEnTraL, and from the CINECA through the award under the ISCRA initiative, for the availability of HPC resources.

Note added. During the final writing of the present work a manuscript by Blakie et al. [32] has reported the calculation of the speeds of sound of a supersolid dipolar gas confined in a infinite tube potential. Their results, based on the solution of the Bogoliubov equations, turn out to be in general agreement with our findings and could be used to obtain the parameters of the hydrodynamic model of supersolids in the thermodynamic limit.

* These 2 authors contributed equally to the paper

† Corresponding Author: alessio.recati@ino.cnr.it

- [1] A. F. Andreev and I. M. Lifshitz, Quantum theory of defects in crystals, *Sov. Phys. JETP* **29**, 1107 (1969).
- [2] C.-D. Yoo and A. T. Dorsey, Hydrodynamic theory of supersolids: Variational principle, effective lagrangian, and density-density correlation function, *Phys. Rev. B* **81**, 134518 (2010).
- [3] J. Hofmann and W. Zwerger, Hydrodynamics of a superfluid smectic, *Journal of Statistical Mechanics: Theory and Experiment* **2021**, 033104 (2021).
- [4] S. Saccani, S. Moroni, and M. Boninsegni, Excitation spectrum of a supersolid, *Phys. Rev. Lett.* **108**, 175301 (2012).
- [5] T. Macrì, F. Maucher, F. Cinti, and T. Pohl, Elementary excitations of ultracold soft-core bosons across the superfluid-supersolid phase transition, *Phys. Rev. A* **87**, 061602 (2013).
- [6] F. Ancilotto, M. Rossi, and F. Toigo, Supersolid structure and excitation spectrum of soft-core bosons in three dimensions, *Phys. Rev. A* **88**, 033618 (2013).
- [7] A. Recati and S. Stringari, Coherently coupled mixtures of ultracold atomic gases, *Annual Review of Condensed Matter Physics* **13**, 407 (2022), <https://doi.org/10.1146/annurev-conmatphys-031820-121316>.
- [8] G. I. Martone, Bose-einstein condensates with raman-induced spin-orbit coupling: An overview, *Europhysics Letters* **143**, 25001 (2023).
- [9] S. M. Roccuzzo and F. Ancilotto, Supersolid behavior of a dipolar bose-einstein condensate confined in a tube, *Phys. Rev. A* **99**, 041601 (2019).
- [10] A. Recati and S. Stringari, To appear in *Nature Perspective* (2023).
- [11] L. Tanzi, S. M. Roccuzzo, E. Lucioni, F. Famà, A. Fioretti, C. Gabbanini, G. Modugno, A. Recati, and S. Stringari, Supersolid symmetry breaking from compressional oscillations in a dipolar quantum gas, *Nature* **574**, 382 (2019).
- [12] M. Guo, F. Böttcher, J. Hertkorn, J.-N. Schmidt, M. Wenzel, H. P. Büchler, T. Langen, and T. Pfau, The low-energy Goldstone mode in a trapped dipolar supersolid, *Nature* **574**, 386 (2019).
- [13] G. Natale, R. M. W. van Bijnen, A. Patscheider, D. Peter, M. J. Mark, L. Chomaz, and F. Ferlaino, Excitation spectrum of a trapped dipolar supersolid and its experimental evidence, *Phys. Rev. Lett.* **123**, 050402 (2019).
- [14] S. M. Roccuzzo, S. Stringari, and A. Recati, Supersolid edge and bulk phases of a dipolar quantum gas in a box, *Phys. Rev. Res.* **4**, 013086 (2022).
- [15] L. Amico, M. Boshier, G. Birkel, A. Minguzzi, C. Miniatura, L.-C. Kwek, D. Aghamalyan, V. Ahufinger, D. Anderson, N. Andrei, A. S. Arnold, M. Baker, T. A. Bell, T. Bland, J. P. Brantut, D. Cassettari, W. J. Chetcuti, F. Chevy, R. Citro, S. De Palo, R. Dumke, M. Edwards, R. Folman, J. Fortagh, S. A. Gardiner, B. M. Garraway, G. Gauthier, A. Günther, T. Haug, C. Hufnagel, M. Keil, P. Ireland, M. Lebrat, W. Li, L. Longchambon, J. Mompert, O. Morsch, P. Naldesi, T. W. Neely, M. Olshanii, E. Orignac, S. Pandey, A. Pérez-Obiol, H. Perrin, L. Piroli, J. Polo, A. L. Pritchard, N. P. Proukakis, C. Rylands, H. Rubinsztein-Dunlop, F. Scazza, S. Stringari, F. Tosto, A. Trombettoni, N. Victorin, W. v. Klitzing, D. Wilkowski, K. Khani, and A. Yakimenko, Roadmap on Atomtronics: State of the art and perspective, *AVS Quantum Science* **3**, 039201 (2021).
- [16] L. Amico, D. Anderson, M. Boshier, J.-P. Brantut, L.-C. Kwek, A. Minguzzi, and W. von Klitzing, Colloquium: Atomtronic circuits: From many-body physics to quantum technologies, *Rev. Mod. Phys.* **94**, 041001 (2022).
- [17] The cloud's shape is influenced by long-ranged dipolar repulsion effectively increasing its radius.
- [18] F. Wächtler and L. Santos, Quantum filaments in dipolar bose-einstein condensates, *Phys. Rev. A* **93**, 061603 (2016).
- [19] A. Kumar, N. Anderson, W. D. Phillips, S. Eckel, G. K. Campbell, and S. Stringari, Minimally destructive, doppler measurement of a quantized flow in a ring-shaped bose-einstein condensate, *New Journal of Physics* **18**, 025001 (2016).
- [20] G. Chauveau, C. Maury, F. Rabec, C. Heintze, G. Brochier, S. Nascimbene, J. Dalibard, J. Beugnon, S. M. Roccuzzo, and S. Stringari, Superfluid fraction in an interacting spatially modulated bose-einstein condensate, *Phys. Rev. Lett.* **130**, 226003 (2023).
- [21] P. M. Chaikin and T. C. Lubensky, *Principles of Condensed Matter Physics* (Cambridge University Press, 1995).
- [22] L.L.Landau, *J. Phys. USSR* **5**, 70 (1941).

- [23] L. Pitaevskii and S. Stringari, *Bose-Einstein condensation and superfluidity* (Oxford University Press, 2016).
- [24] P. C. Martin, O. Parodi, and P. S. Pershan, Unified hydrodynamic theory for crystals, liquid crystals, and normal fluids, *Phys. Rev. A* **6**, 2401 (1972).
- [25] W.F.Vinen, *Physics of Quantum Fluids*, ed. by R. Kubo and F. Takano (Syokabo Publishing Company, Tokyo, 1970).
- [26] H. Hu, E. Taylor, X.-J. Liu, S. Stringari, and A. Griffin, Second sound and the density response function in uniform superfluid atomic gases, *New Journal of Physics* **12**, 043040 (2010).
- [27] L. Santos, G. V. Shlyapnikov, and M. Lewenstein, Roton-maxon spectrum and stability of trapped dipolar bose-einstein condensates, *Phys. Rev. Lett.* **90**, 250403 (2003).
- [28] D. Petter, G. Natale, R. M. W. van Bijnen, A. Patscheider, M. J. Mark, L. Chomaz, and F. Ferlaino, Probing the roton excitation spectrum of a stable dipolar bose gas, *Phys. Rev. Lett.* **122**, 183401 (2019).
- [29] Ring configurations of similar shape, hosting a supersolid dipolar gas with persistent currents, were considered in [33].
- [30] The energy dependence on angular momentum for such rotating configurations at larger Ω has recently been explored in [33].
- [31] The good agreement between Leggett's upper bound and the superfluid fraction calculated in an infinite tube by means of effective mass was recently discussed in [34].
- [32] P. B. Blakie, L. Chomaz, D. Baillie, F. Ferlaino, arXiv:2306.04794 (2023).
- [33] M. N. Tengstrand, D. Bohlm, R. Sachdeva, J. Bengtsson, and S. M. Reimann, Persistent currents in toroidal dipolar supersolids, *Phys. Rev. A* **103**, 013313 (2021).
- [34] J. C. Smith, D. Baillie, and P. B. Blakie, Supersolidity and crystallization of a dipolar bose gas in an infinite tube, *Phys. Rev. A* **107**, 033301 (2023).

Creation and robustness of quantized vortices in a dipolar supersolid when crossing the superfluid-to-supersolid transition

Marija Šindik ^{1,2}, Alessio Recati,^{1,3,*} Santo Maria Rocuzzo,⁴ Luis Santos,^{5,†} and Sandro Stringari^{1,3}

¹*Pitaevskii BEC Center, CNR-INO and Dipartimento di Fisica, Università di Trento, 38123 Trento, Italy*

²*Institute of Physics Belgrade, University of Belgrade, 11080 Belgrade, Serbia*

³*Trento Institute for Fundamental Physics and Applications, INFN, 38123 Trento, Italy*

⁴*Kirchhoff-Institut für Physik, Ruprecht-Karls-Universität Heidelberg, 69120 Heidelberg, Germany*

⁵*Institut für Theoretische Physik, Leibniz Universität Hannover, 30167 Hannover, Germany*

 (Received 29 June 2022; revised 23 August 2022; accepted 5 December 2022; published 21 December 2022)

We study quantized vortices in dipolar supersolids at the transition between the superfluid and the supersolid phase. We present an approach to the nucleation of vortices and their observation, based on the quenching of the s -wave scattering length across the phase transition. Starting from a slowly rotating, vortex-free configuration in the superfluid phase, we predict vortex nucleation as the system enters the supersolid phase, due to the strong reduction of the critical angular velocity in the supersolid. Once a vortex is created, we show that it is robustly preserved when the condensate is brought back to the superfluid phase, where it may be readily observed. These results may have a significant impact on ongoing experiments, given that the observation of quantized vortices would constitute a key probe of the superfluid character of dipolar supersolids.

DOI: [10.1103/PhysRevA.106.L061303](https://doi.org/10.1103/PhysRevA.106.L061303)

Quantized vortices constitute a key hallmark of superfluidity [1]. They are topological defects of the order parameter, and therefore robust with respect to perturbations in the $U(1)$ broken symmetry phase. Ultracold gases are an ideal platform for the study of vortices. In these gases, vortices are typically created either by stirring the cloud with a laser, or by rotating a slightly deformed trap. Vortices are detected, after a condensate expansion, by the observation of the density holes corresponding to the vortex cores. Vortices have been observed both in Bose-Einstein condensates (BECs) [2–4] and in superfluid spin-1/2 Fermi gases [5]. The angular momentum and its quantization in the presence of a vortex can be inferred by exploiting the lift in the degeneracy of quadrupole-mode frequencies due to broken time-reversal symmetry [6], as observed in condensates [7,8].

Supersolids constitute a particularly intriguing phase in which superfluidity coexists with a modulated density [9]. In the last few years, supersolidity has attracted major attention in ultracold gases. Experiments on BECs in optical cavities have revealed supersolidlike properties [10]. Condensates with an imposed one-dimensional spin-orbit coupling have been shown to present a supersolid stripe phase [11,12]. Recent experiments on BECs of magnetic atoms have revealed the creation of supersolids of ultradilute droplets maintained by the interplay between attractive mean-field interactions and the effective repulsion induced by quantum fluctuations [13]. Dipolar supersolids have attracted quickly growing interest, and successful experiments in droplet arrays have studied the phase coherence [14–17], the appearance of Goldstone

modes in the excitation spectrum [18–20], and the peculiar dynamics related to scissors modes [21–24]. Very recently, two-dimensional supersolid configurations have been also realized [25,26].

Recent theoretical works have investigated quantum vortices in dipolar supersolids [27,28]. Quantum vortices in a supersolid were first discussed in Ref. [29] in the context of a hypothetical supersolid phase of helium. There it was shown, in the context of a mean-field Gross-Pitaevskii formalism employing a repulsive soft-core interaction, that vortices may be nucleated in the supersolid by an obstacle. It was suggested as well that vortices could be robust when crossing back and forth the superfluid-to-supersolid transition. A peculiar feature pointed out in Ref. [27] in the case of supersolid dipolar gases is that vortices are, both energetically and dynamically, more favored in the supersolid phase than in the superfluid one. The low-density regions surrounding the droplets of the supersolid phase help in reducing the energetic barrier for a vortex to enter the system, and in pinning the vortices in the interstitials between droplets [27]. Even a very slow rotation of the trapping potential can then trigger the dynamical instability that drives vortex nucleation [27]. However, the direct detection of vortices formed in the interstitials is largely inhibited because, even in the absence of vortices, this region is characterized by a very low density.

In this Letter, we first explore in detail the robustness of vortices in dipolar BECs when crossing the superfluid-to-supersolid transition, showing that the conservation of angular momentum results in a peculiar dynamic behavior, since the value of the angular momentum per particle associated to a vortex is markedly different in the superfluid and in the supersolid phase. Using the difference in the vortex properties in both phases, we propose a dynamic protocol based on the

*Corresponding author: alessio.recati@ino.it

†Corresponding author: santos@itp.uni-hannover.de

quench of a slowly rotating dipolar condensate from the superfluid into the supersolid phase. A vortex is nucleated in the supersolid due to the strongly reduced critical angular velocity, and a subsequent quench back allows for straightforward vortex imaging in the superfluid phase. Our protocol could provide not only the experimental proof of vortex nucleation in a dipolar supersolid, but also allows for directly probing the modified vortex properties in that phase [27], as, e.g., the reduction of the critical angular velocity for vortex nucleation. It has the advantage of avoiding the nucleation of vortices starting from the equilibrium configuration in the supersolid phase, whose implementation is notoriously more difficult due to three-body collisions.

Model. We consider a BEC of atoms with mass m and magnetic dipole moment μ aligned along the z axis, trapped in a harmonic potential of the form $V_{\text{ext}}(\mathbf{r}) = m\omega_{\perp}^2[(1 - \varepsilon)x^2 + (1 + \varepsilon)y^2 + \lambda^2 z^2]/2$.

At zero temperature the physics of the system is well described by the extended Gross-Pitaevskii equation (eGPE) [30,31],

$$i\hbar \frac{\partial \Psi(\mathbf{r}, t)}{\partial t} = \left[-\frac{\hbar^2 \nabla^2}{2m} + V_{\text{ext}}(\mathbf{r}) + g|\Psi(\mathbf{r}, t)|^2 + \int d\mathbf{r}' V_{dd}(\mathbf{r} - \mathbf{r}') |\Psi(\mathbf{r}', t)|^2 + \gamma |\Psi(\mathbf{r}, t)|^3 \right] \Psi(\mathbf{r}, t), \quad (1)$$

where $g = 4\pi\hbar^2 a/m > 0$ is the coupling constant fixed by the s -wave scattering length a , and $V_{dd}(\mathbf{r}) = \frac{\mu_0 \mu^2}{4\pi} \frac{1 - 3\cos^2\theta}{|\mathbf{r}|^3}$ is the dipole-dipole interaction, with θ the angle between \mathbf{r} and the z axis. The last term in Eq. (1) is given by the repulsive Lee-Huang-Yang (LHY) correction induced by quantum fluctuations, with

$$\gamma = \frac{32ga^3/2}{3\sqrt{\pi}} \text{Re} \left[\int_0^1 du [1 + \epsilon_{dd}(3u^2 - 1)]^{5/2} \right], \quad (2)$$

where $\epsilon_{dd} = \mu_0 \mu^2 / 3g$ characterizes the relative strength of the dipolar interaction with respect to the contact one. The eGPE has been systematically employed in the last few years to investigate quantum droplets and supersolidity in dipolar BECs [13].

For small-enough ϵ_{dd} , the system behaves as a standard condensate (superfluid phase). By decreasing the scattering length, and hence increasing the value of ϵ_{dd} , the role of the attractive part of the dipolar force becomes more important, and the LHY term starts playing a crucial role in determining the equilibrium solution. The LHY term ensures the stability of the system against collapse and eventually favors the formation of a periodic structure, which can be regarded as a series of dense droplets connected by a dilute superfluid gas (supersolid phase) [14–16]. A further increase of ϵ_{dd} leads to a state where the droplets are independent and mutually incoherent, and the system does not show any extended superfluidity (independent droplet phase).¹

The supersolid phase can host quantized vortices [27]. As already anticipated in the Introduction, vortex nucleation is significantly favored by the reduced density in the interdroplet regions, but vortices nestle in those interstitials, making their experimental observation much more problematic than in the superfluid phase. Below, we first discuss the robustness of vortices when quenching the system across the superfluid-to-supersolid transition. We then exploit such a robustness to design a protocol that first allows for an alternative mechanism for the nucleation of vortices in the supersolid phase and, second, for probing their existence by imaging them in the superfluid phase, where they are more easily detectable, also owing to the large increase of their core size as compared to condensates with only contact interactions. This second step resembles the procedure used in the pioneering work of Ref. [5], where the vortices created in a strongly interacting Fermi gas were imaged by quenching from the BCS to the BEC regime, where their visibility was better ensured after gas expansion. In the case of dipolar gases the procedure is more challenging because the two regimes, supersolid and superfluid, are separated by a first-order phase transition and not connected by a continuous crossover.

Crossing the superfluid-to-supersolid transition. We consider a BEC of 4×10^4 ¹⁶⁴Dy atoms, confined in an axially symmetrical trap ($\varepsilon = 0$) with $\omega_{\perp} = 2\pi \times 60$ Hz and $\lambda = 2$. Under these conditions, the superfluid-to-supersolid transition occurs at the value $a_{\text{crit}} = 94.6a_0$ (a_0 is the Bohr radius) corresponding to $\epsilon_{dd} = 1.395$.

Ground states of the system are calculated using imaginary-time evolution in the rotating frame, obtained by adding the constraint $-\Omega L_z$ to the eGPE (1), where Ω is the angular velocity, and L_z the z component of the angular momentum operator.² Above some critical angular velocity Ω_c , vortical solutions become energetically favorable. It is important to notice that Ω_c is significantly smaller than the one required for the dynamical vortex nucleation [27], associated with a quadrupolar instability, as we discuss later.

We first consider a vortex in the superfluid phase, obtained for $a = 105a_0 > a_{\text{crit}}$, and $\Omega = 0.22\omega_{\perp} > \Omega_c$ [see Fig. 1(a)(i)]. In the superfluid phase the vortex is characterized by an angular momentum \hbar per particle. Starting from this ground-state configuration,³ we ramp down in 100 ms the s -wave scattering length to a value $a = 94a_0 < a_{\text{crit}}$, which would correspond at equilibrium to the supersolid phase. Indeed, once the transition is crossed, a strong density modulation emerges on a very short timescale, leading to the formation of droplets. After a certain waiting time the system acquires a configuration close to the ground-state shape with a vortex in the supersolid phase [Fig. 1(a)(iii)]. It is, however, interesting to notice that in most cases we find a transient regime [see Fig. 1(a)(ii)] where the number of peaks is larger (four droplets) than in the final, ground-state-like configuration (three droplets). Despite the occurrence of small

²The critical value a_{crit} increases slightly by increasing Ω . Such a change is, however, less than 0.5% for the angular velocities used in this text.

³All the time-dependent simulations presented in this Letter are performed in the laboratory reference frame.

¹Notice, however, that each droplet is still superfluid.

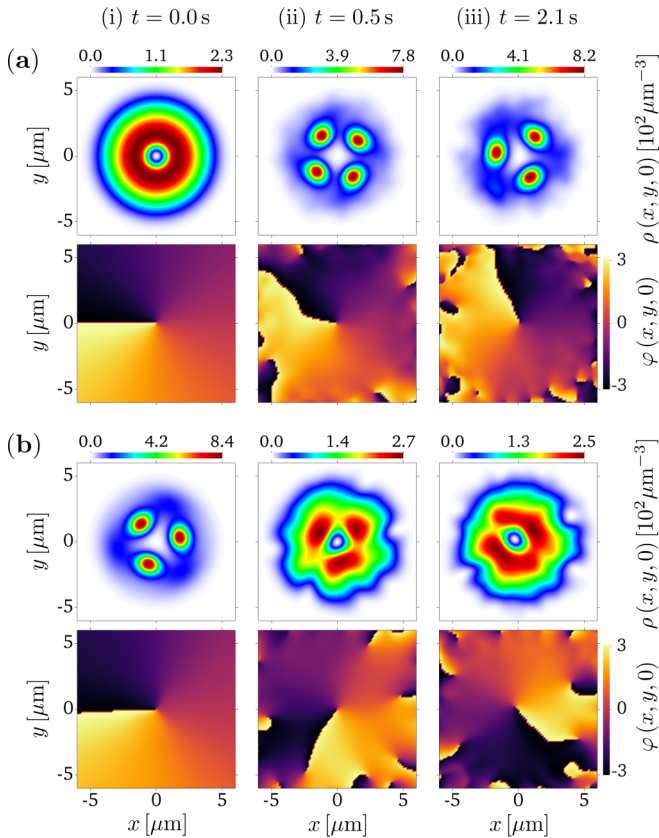


FIG. 1. Density and phase profiles in the $z = 0$ plane. (a) Vortex through the superfluid-to-supersolid crossing at $t = 0, 0.5$, and 2.1 s. The vortex is initially created in the superfluid regime ($\Omega/\omega_{\perp} = 0.22$, $a = 105a_0$), and a is then linearly ramped in 100 ms down to $94a_0$, within the supersolid phase. (b) Vortex through the supersolid-to-superfluid crossing for the same times. At $t = 0$, the vortex is in the supersolid phase ($\Omega/\omega_{\perp} = 0.16$, $a = 94a_0$). Then a is ramped in 100 ms up to $105a_0$, within the superfluid regime. In all cases, $\omega_{\perp} = 2\pi \times 60$ Hz, $\lambda = 2$, and $\varepsilon = 0$.

oscillations caused by the crossing of the first-order transition, the vortex survives at the trap center, with its characteristic phase pattern. Since angular momentum is conserved during the ramping of the scattering length, and since in the supersolid the angular momentum per particle carried by the vortex is smaller than \hbar due to the reduced global superfluidity [27], the remaining angular momentum is carried by the droplets, whose centers of mass rotate in the laboratory frame with an angular velocity larger than Ω .

Crossing the supersolid-to-superfluid transition. We carry out the same analysis in the opposite direction, following the fate of a quantized vortex initially present in the supersolid phase, an especially relevant case for the protocol discussed below. As discussed in Ref. [27], the angular velocity Ω_c , for which the vortex becomes energetically favorable, is much smaller than the one in the superfluid phase. In Fig. 1(b)(i), we consider a configuration with $a = 94a_0$ and $\Omega = 0.16\omega_{\perp}$, slightly higher than the critical value Ω_c . The created vortex is characterized by an angular momentum per particle of $0.87\hbar$. After ramping in 100 ms the scattering length up to $a = 105a_0$ to reach the superfluid phase, we find that the vortex remains

clearly visible [Figs. 1(b)(ii) and 1(b)(iii)]. Note, however, that the density profile preserves some density modulations, which are the residue of the original droplets characterizing the supersolid phase. Moreover, since the overall angular momentum must be preserved, the larger angular momentum associated with the vortex in the superfluid phase (\hbar) is compensated by the rotational motion of the density modulations, and by the occurrence of antivortices located near the border of the atomic cloud, as well as, in some cases, by a slight displacement of the vortex core from the center of the trap.

Protocol for vortex nucleation and detection. We are now ready to discuss our protocol which combines the favorable nucleation mechanism of quantized vortices exhibited by the supersolid phase with their topological robustness when the supersolid-to-superfluid phase transition is crossed. Our starting point is a slowly rotating trapped dipolar gas in the superfluid phase ($a = 105a_0$), obtained by a sudden introduction of rotation to the superfluid ground state in a slightly deformed trap in the xy plane, and letting it equilibrate for 200 ms [see Fig. 2(a)]. In the laboratory frame this corresponds to choosing a harmonic potential of the form

$$V_{\text{ext}}(t) = \frac{m}{2}\omega_{\perp}^2\{(1 - \varepsilon)[x \cos(\Omega t) + y \sin(\Omega t)]^2 + (1 + \varepsilon)[-x \sin(\Omega t) + y \cos(\Omega t)]^2 + \lambda^2 z^2\}. \quad (3)$$

We choose a slightly deformed trap ($\varepsilon = 6.6\%$) and an angular velocity ($\Omega = 0.3\omega_{\perp}$) such that the system is unable to nucleate vortices in the superfluid phase, as the quadrupole dynamical instability occurs at $0.45\omega_{\perp}$.⁴ The parameters are instead large enough for vortex nucleation once the system enters the supersolid phase. Therefore we reduce the value of the scattering length with a linear ramp in 100 ms down to $a = 94a_0$. After entering the supersolid phase, first droplets are formed [Fig. 2(b)] and, after a while, a vortex is nucleated in the center [Fig. 2(c)]. Notice that the timescale for this process is slow in the present simulation. We expect, however, that in a real experimental situation the timescale will be much faster, as a consequence of thermal noise, which is not accounted for in our calculations. When the vortex is formed [Fig. 2(c)] we restore the isotropy of the trap ($\varepsilon = 0$) in order to ensure the robustness of the topological configuration associated with the vortex and the conservation of angular momentum. We ramp the scattering length back to its initial value (following a similar ramp) and after a while [Fig. 2(d)] the system enters again the superfluid phase. We then recover a very similar configuration as that of Fig. 1(b)(iii).

The same protocol may be employed for the nucleation of more than one vortex when increasing the angular velocity Ω of the rotating trap. In Fig. 3, we show our results for different angular velocities in our protocol. The upper panel shows the atomic cloud in the supersolid phase right before inverting the ramping of the scattering length. The lower panel depicts the final density distribution after ramping back the scattering length. The case with $\Omega = 0$ is important, since it clearly shows that despite the strong density modulation in the supersolid regime, once moving back into the superfluid no

⁴This value remains almost constant in the whole superfluid region.

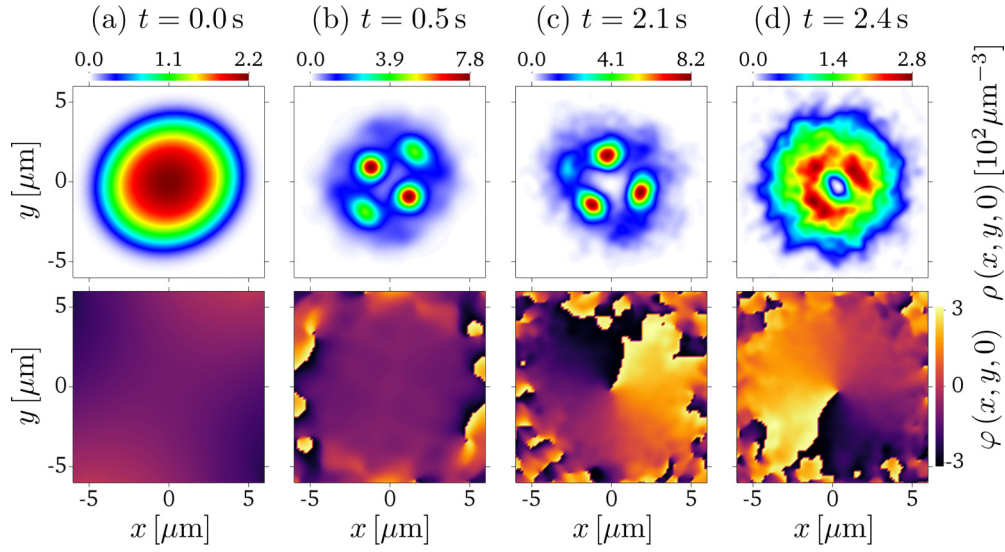


FIG. 2. Density and phase profiles in the $z = 0$ plane, showing vortex nucleation employing the protocol discussed in the text. (a) Initial vortex-free superfluid with a scattering length $a = 105a_0$, confined in a slightly deformed harmonic trap ($\omega_{\perp} = 2\pi \times 60$ Hz, $\lambda = 2$, $\varepsilon = 6.6\%$), rotating with an angular velocity $\Omega = 0.3\omega_{\perp}$. (b) The scattering length is linearly ramped in 100 ms down to $a_s = 94a_0$, resulting in a transition to the supersolid phase. (c) After some time a vortex is nucleated at the center of the trap. (d) The isotropy of the trap is restored ($\varepsilon = 0$) and the scattering length is linearly ramped in 100 ms up to the initial value, resulting in a superfluid with a readily detectable vortex core.

core appears, the final density remains smooth and characterized by a maximum in the center, very similar to the initial equilibrium configuration. By increasing Ω we eventually observe one vortex nucleated in the center using $\Omega = 0.3\omega_{\perp}$ [same as Figs. 2(c) and 2(d)], two vortices using $\Omega = 0.35\omega_{\perp}$, and three vortices using $\Omega = 0.4\omega_{\perp}$. Note that in all cases the vortices are nucleated in the supersolid phase, since the

angular velocity is not large enough to create vortices in the superfluid.

Conclusions. We have studied vortices in a dipolar condensate when crossing the superfluid-to-supersolid transition. We have proposed in particular a protocol that should permit under realistic conditions to nucleate and detect quantized vortices in a dipolar supersolid, a major hallmark of

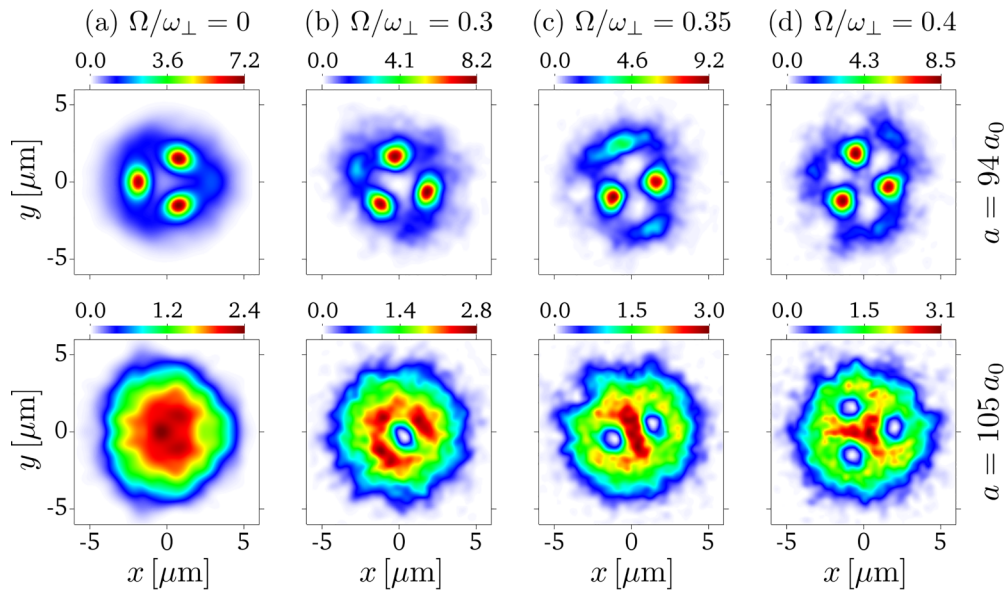


FIG. 3. Density profiles in the $z = 0$ plane. Results for the dynamical protocol for different angular velocities: $\Omega/\omega_{\perp} = 0$ (a), 0.3 (b), 0.35 (c), and 0.4 (d). The parameters and procedure are the same as in Fig. 2. The upper row corresponds to the configurations in the supersolid phase at $t = 2.1$ s, before inverting the ramp of the scattering length. The lower row corresponds to the final configuration in the superfluid phase (at $t = 2.4$ s) after ramping back the scattering length. Note that imaging in the superfluid phase should easily reveal the presence of no vortex, one, two, and three vortices, respectively. The final angular momentum per particle (once the isotropy of the xy trapping is restored) is (a) $L = 0$, (b) $L = 1.03\hbar$, (c) $L = 1.85\hbar$, and (d) $L = 2.42\hbar$.

superfluidity. The method is based on a controlled ramp of the scattering length across the superfluid-to-supersolid transition, employing the very nature of the supersolid to induce vortex nucleation. Although vortex detection is difficult in the supersolid since vortices gather in regions of very low density, a ramp back into the superfluid permits an easy imaging of the vortex core, even more so than in contact-interacting condensates due to the significantly larger vortex size in a dipolar BEC. Very recently, quantized vortices have been actually observed in the superfluid phase of a dipolar gas [32,33].

Acknowledgments. We thank A. Gallemí for interesting discussions. This work was supported by Q@TN (the joint laboratory between University of Trento, FBK - Fondazione Bruno Kessler, INFN - National Institute for Nuclear

Physics, and CNR - National Research Council) and the Provincia Autonoma di Trento. L.S. acknowledges support of the Deutsche Forschungsgemeinschaft (DFG, German Research Foundation) under Germany's Excellence Strategy – EXC-2123 QuantumFrontiers – 390837967, and FOR 2247. S.M.R. acknowledges support from the Alexander von Humboldt Foundation. A.R. acknowledges support of the Italian MUR under the PRIN2017 project CEnTraL (Protocol No. 20172H2SC4). M.S. acknowledges funding provided by the Institute of Physics Belgrade, through the grant by the Ministry of Education, Science, and Technological Development of the Republic of Serbia. We acknowledge the CINECA award under the ISCRA initiative, for the availability of high-performance computing resources and support.

-
- [1] L. Pitaevskii and S. Stringari, *Bose-Einstein Condensation and Superfluidity* (Oxford University Press, Oxford, UK, 2016).
- [2] M. R. Matthews, B. P. Anderson, P. C. Haljan, D. S. Hall, C. E. Wieman, and E. A. Cornell, *Phys. Rev. Lett.* **83**, 2498 (1999).
- [3] K. W. Madison, F. Chevy, W. Wohlleben, and J. Dalibard, *Phys. Rev. Lett.* **84**, 806 (2000).
- [4] J. R. Abo-Shaeer, C. Raman, J. M. Vogels, and W. Ketterle, *Science* **292**, 476 (2001).
- [5] M. W. Zwierlein, J. R. Abo-Shaeer, A. Schirotzek, C. H. Schunck, and W. Ketterle, *Nature (London)* **435**, 1047 (2005).
- [6] F. Zambelli and S. Stringari, *Phys. Rev. Lett.* **81**, 1754 (1998).
- [7] F. Chevy, K. W. Madison, and J. Dalibard, *Phys. Rev. Lett.* **85**, 2223 (2000).
- [8] P. C. Haljan, I. Coddington, P. Engels, and E. A. Cornell, *Phys. Rev. Lett.* **87**, 210403 (2001).
- [9] M. Boninsegni and N. V. Prokof'ev, *Rev. Mod. Phys.* **84**, 759 (2012).
- [10] J. Léonard, A. Morales, P. Zupancic, T. Esslinger, and T. Donner, *Nature (London)* **543**, 87 (2017).
- [11] J.-R. Li, J. Lee, W. Huang, S. Burchesky, B. Shteynas, F. Ç. Top, A. O. Jamison, and W. Ketterle, *Nature (London)* **543**, 91 (2017).
- [12] K. T. Geier, G. I. Martone, P. Hauke, and S. Stringari, *Phys. Rev. Lett.* **127**, 115301 (2021).
- [13] F. Böttcher, J.-N. Schmidt, J. Hertkorn, K. S. H. Ng, S. D. Graham, M. Guo, T. Langen, and T. Pfau, *Rep. Prog. Phys.* **84**, 012403 (2020).
- [14] L. Tanzi, E. Lucioni, F. Famà, J. Catani, A. Fioretti, C. Gabbanini, R. N. Bisset, L. Santos, and G. Modugno, *Phys. Rev. Lett.* **122**, 130405 (2019).
- [15] F. Böttcher, J.-N. Schmidt, M. Wenzel, J. Hertkorn, M. Guo, T. Langen, and T. Pfau, *Phys. Rev. X* **9**, 011051 (2019).
- [16] L. Chomaz, D. Petter, P. Ilzhöfer, G. Natale, A. Trautmann, C. Politi, G. Durastante, R. M. W. van Bijnen, A. Patscheider, M. Sohmen *et al.*, *Phys. Rev. X* **9**, 021012 (2019).
- [17] P. Ilzhöfer, M. Sohmen, G. Durastante, C. Politi, A. Trautmann, G. Natale, G. Morpurgo, T. Giamarchi, L. Chomaz, M. J. Mark *et al.*, *Nat. Phys.* **17**, 356 (2021).
- [18] L. Tanzi, S. M. Roccuzzo, E. Lucioni, F. Famà, A. Fioretti, C. Gabbanini, G. Modugno, A. Recati, and S. Stringari, *Nature (London)* **574**, 382 (2019).
- [19] M. Guo, F. Böttcher, J. Hertkorn, J.-N. Schmidt, M. Wenzel, H. P. Büchler, T. Langen, and T. Pfau, *Nature (London)* **574**, 386 (2019).
- [20] G. Natale, R. M. W. van Bijnen, A. Patscheider, D. Petter, M. J. Mark, L. Chomaz, and F. Ferlaino, *Phys. Rev. Lett.* **123**, 050402 (2019).
- [21] I. Ferrier-Barbut, M. Wenzel, F. Böttcher, T. Langen, M. Isoard, S. Stringari, and T. Pfau, *Phys. Rev. Lett.* **120**, 160402 (2018).
- [22] L. Tanzi, J. G. Maloberti, G. Biagioni, A. Fioretti, C. Gabbanini, and G. Modugno, *Science* **371**, 1162 (2021).
- [23] M. A. Norcia, E. Poli, C. Politi, L. Klaus, T. Bland, M. J. Mark, L. Santos, R. N. Bisset, and F. Ferlaino, *Phys. Rev. Lett.* **129**, 040403 (2022).
- [24] S. M. Roccuzzo, A. Recati, and S. Stringari, *Phys. Rev. A* **105**, 023316 (2022).
- [25] M. A. Norcia, C. Politi, L. Klaus, E. Poli, M. Sohmen, M. J. Mark, R. N. Bisset, L. Santos, and F. Ferlaino, *Nature (London)* **596**, 357 (2021).
- [26] T. Bland, E. Poli, C. Politi, L. Klaus, M. A. Norcia, F. Ferlaino, L. Santos, and R. N. Bisset, *Phys. Rev. Lett.* **128**, 195302 (2022).
- [27] A. Gallemí, S. M. Roccuzzo, S. Stringari, and A. Recati, *Phys. Rev. A* **102**, 023322 (2020).
- [28] F. Ancilotto, M. Barranco, M. Pi, and L. Reatto, *Phys. Rev. A* **103**, 033314 (2021).
- [29] Y. Pomeau and S. Rica, *Phys. Rev. Lett.* **72**, 2426 (1994).
- [30] A. R. P. Lima and A. Pelster, *Phys. Rev. A* **86**, 063609 (2012).
- [31] F. Wächtler and L. Santos, *Phys. Rev. A* **93**, 061603(R) (2016).
- [32] L. Klaus, T. Bland, E. Poli, C. Politi, G. Lamporesi, E. Casotti, R. N. Bisset, M. J. Mark, and F. Ferlaino, *Nat. Phys.* **18**, 1453 (2022).
- [33] Z. Hadzibabic, *Nat. Phys.* **18**, 1393 (2022).

XUV-driven plasma switch for THz: new spatio-temporal overlap tool for XUV–THz pump–probe experiments at FELs¹

E. Zapolnova,^a R. Pan,^a T. Golz,^a M. Sindik,^a M. Nikolic,^a M. Temme,^a
M. Rabasovic,^b D. Grujic,^b Z. Chen,^c S. Toleikis^a and N. Stojanovic^{a,*}

Received 5 February 2019

Accepted 16 October 2019

Edited by J. Grünert, European XFEL, Germany

¹This article will form part of a virtual special issue containing papers presented at the PhotonDiag2018 workshop.

Keywords: plasma switch; XUV; pump–probe; temporal overlap.

^aDeutsches Elektronen-Synchrotron (DESY), Notkestrasse 85, 22607 Hamburg, Germany, ^bInstitute of Physics Belgrade, Pregrevica 118, 11080 Belgrade, Serbia, and ^cSLAC National Accelerator Laboratory, Menlo Park, CA 94025, USA.

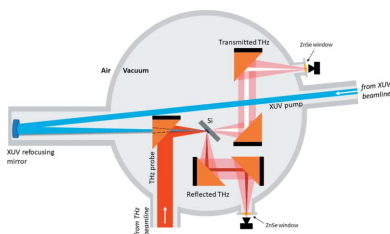
*Correspondence e-mail: nikola.stojanovic@desy.de

A simple and robust tool for spatio-temporal overlap of THz and XUV pulses in in-vacuum pump–probe experiments is presented. The technique exploits ultrafast changes of the optical properties in semiconductors (*i.e.* silicon) driven by ultrashort XUV pulses that are probed by THz pulses. This work demonstrates that this tool can be used for a large range of XUV fluences that are significantly lower than when probing by visible and near-infrared pulses. This tool is mainly targeted at emerging X-ray free-electron laser facilities, but can be utilized also at table-top high-harmonics sources.

1. Introduction

Intense THz pulses combined with synchronized X-ray pulses enable investigation of the dynamics of the light–matter interaction, non-linear response of materials and control of the properties of matter selectively on femtosecond time scales. Therefore, achieving the temporal overlap between pump and probe pulses in the femtosecond range is essential. Certain pump–probe schemes, *e.g.* THz streaking (Frühling *et al.*, 2009; Schmid *et al.*, 2019), are comparatively tolerant against the spatial overlap between XUV and THz pulses and the actual focal position of the THz beam. The observable, *i.e.* the kinetic energy of the photoelectrons, is furthermore of considerable magnitude and can be utilized for further optimization of the pump–probe signal. This is almost never the case in pump–probe experiments on solid-state samples, utilizing one of the XUV probing techniques [*e.g.* X-ray magnetic circular dichroism (XMCD) (Pfau *et al.*, 2012; Willems *et al.*, 2015) and resonant inelastic X-ray scattering (Dell’Angela *et al.*, 2016)]. There, the spatio-temporal overlap between THz and XUV and in particular diffraction-limited focusing of the THz beam have to be achieved with the aid of versatile in-vacuum diagnostics.

The so-called plasma-switch, the transient change of optical constants in the visible (VIS) and near-infrared (NIR) spectral ranges by X-ray and XUV pulses, has been used for the temporal characterization of these pulses (Harmand *et al.*, 2012; Gahl *et al.*, 2008; Krupin *et al.*, 2012; Riedel *et al.*, 2013; Danailov *et al.*, 2014). Transient changes of optical properties in the THz range, driven by femtosecond laser pulses, have been used for pickup of individual pulses from MHz trains at infrared free-electron lasers (FELs) (Schmidt *et al.*, 2015) as well as for THz spectral shaping at table-top THz sources (Cartella *et al.*, 2014; Mayer *et al.*, 2014).



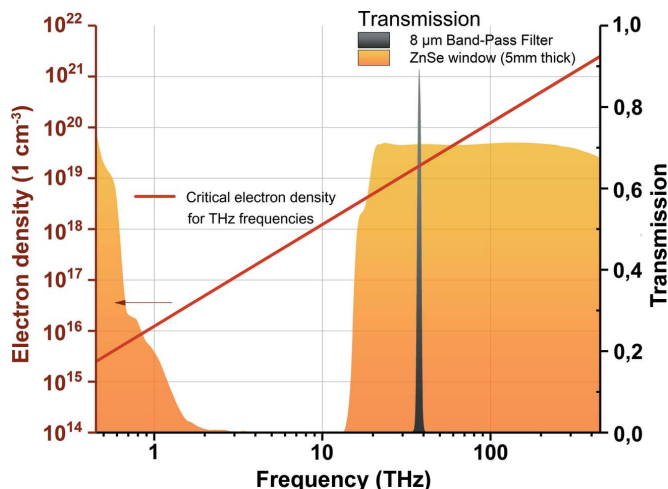


Figure 1
Calculation of the critical electron density for the THz range (red line). Transmission of the 5 mm-thick ZnSe vacuum window and the bandpass filter (at 8 μm wavelength) used in the experiment are presented as the shadowed areas.

As shown in Fig. 1, for lower probing frequencies the effect of the plasma switch is more efficient because lower electron density is required to change the material reflectivity. In this work we present a technique to establish the temporal overlap between XUV and THz pulses, based on the transient change of optical properties of a silicon target in the THz spectral range, induced by the intense femtosecond XUV pulse.

The presented method can be applied in facilities employing THz radiation for time-resolved XUV–THz pump–probe experiments where it is necessary to temporally overlap XUV and THz pulses on a sub-picosecond level.

2. XUV driven THz plasma switch: theoretical background

The process of electronic excitation of materials by an intense XUV pulse happens on an ultrafast time scale, within a few femtoseconds (Gahl *et al.*, 2008; Riedel *et al.*, 2013), and is governed by the photoionization of the electrons in the material: photoabsorption of the bound electrons within the valence band, secondary processes as elastic and inelastic scattering of free electrons, Auger decay, and electron pair creation. Other processes may contribute to the photoionization depending on the energy of the incoming photon and the material (Medvedev & Rethfeld, 2010). Previous theoretical studies have shown that the density of the created free electrons follows the photon flux of the XUV pulse linearly (Riedel *et al.*, 2013) in a wide intensity range, below fluences required for the sample melting, ablation and plasma formation.

Optical properties of the photo-excited material strongly depend on the density of free electrons and can be modelled [e.g. via the continuity equation (Mezentsev *et al.*, 2007)] and expressed in terms of relative permittivity. According to the Drude model, free electrons in a material can be treated as free-electron plasma with a corresponding plasma frequency

ω_p (Ashcroft & Mermin, 1976). We assume that the damping can be neglected in our case (refer to Appendix A for a short discussion on this topic) and the relative permittivity ϵ in this case can be presented as a function of the incoming frequency ω and the plasma frequency ω_p ,

$$\epsilon(\omega) = 1 - \frac{\omega_p^2}{\omega^2}.$$

This indicates that light with a higher frequency than the plasma frequency, $\omega > \omega_p$, can penetrate the plasma whereas light with lower frequency, $\omega < \omega_p$, will be reflected. Taking into account the oscillatory motion of the electron, the critical electron density, n_c , required to make the sample reflective to light with a certain frequency can be presented as

$$n_c = \frac{\epsilon_0 m_e}{e^2} \omega_p^2,$$

where ϵ_0 is the vacuum permittivity, e is the charge and m_e is the mass of an electron.

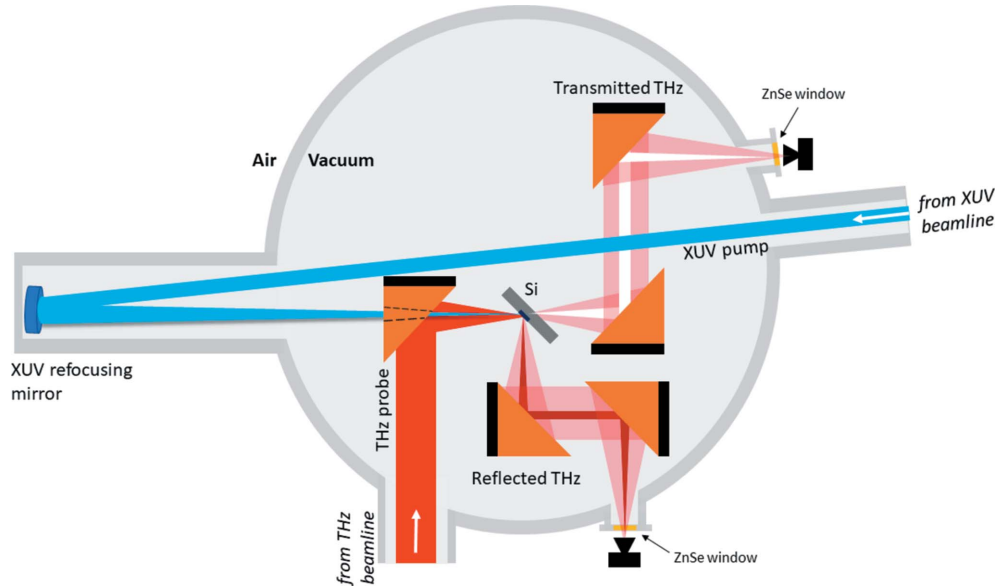
In our experiment, the critical electron density for the probing pulse at a wavelength of 8 μm (37.5 THz) is $n_{c,8\mu\text{m}} = 1.8 \times 10^{19} \text{ cm}^{-3}$, and at wavelengths over 100 μm (<3 THz) it is less than $n_{c,100\mu\text{m}} = 1.1 \times 10^{17} \text{ cm}^{-3}$.

3. Description of the setup

The experiment was performed with the pump XUV wavelength at 13.5 nm (91.8 eV) and two different probing conditions: (i) a THz pulse with a central wavelength of 8 μm, and (ii) a broadband THz pulse with a wavelength >100 μm. The expected pulse duration for THz was ~300 fs and ~3 ps, respectively, and the XUV pulse duration was 160 fs, estimated by electron bunch length measurements by a transverse deflecting RF-structure (Düsterer *et al.*, 2014).

The THz beam is collimated using five toroidal mirrors in order to keep the beam size within the range of the beam transport and optics. This additional folding of the THz beam results in a ~6.5 m longer optical path with respect to the XUV beam. In order to overlap the XUV and THz pulses in time, an additional delay for the XUV is introduced: pulses travel 3.25 m longer distance and then are refocused by a mirror with 3.5 m focal length back to the experiment (Pan *et al.*, 2019). The scheme of the experiment is presented in Fig. 2.

The THz and XUV pulses are collinearly focused and spatially overlapped in the experimental chamber on a 400 μm-thick Si sample at a 45° incident angle. The transmitted and reflected portions of the THz beam are picked up and collimated using parabolic mirrors. Then they are focused through ZnSe vacuum windows (5 mm thick) on two 2 mm × 2 mm pyro detectors (InfraTec LME-301) located outside of the experimental chamber in air ~5 mm from the window. The detectors were custom-designed by collaboration of the DESY FLA group and InfraTec to reduce internal THz interferences (Wesch, 2012). The detectors are without optical windows, which makes them suitable for measurements along a broad spectral range and sensitive to XUV radiation. ZnSe


Figure 2

Scheme of the XUV-driven plasma switch experiment for the THz beam. The THz and XUV beams are collinearly focused and spatially overlapped on a 400 μm -thick Si sample at a 45° incidence angle. Transmitted and reflected THz beams are picked up by off-axis parabolic mirrors and further focused on the corresponding pyro detectors through 5 mm-thick ZnSe vacuum windows.

Table 1

Transmission of XUV at 13.5 nm.

XUV pulse energy via GMD	112 $\mu\text{J} \pm 17 \mu\text{J}$
Beamline transmission	78%
Refocusing mirror	62%
Si ₃ N ₄ 500 nm filter transmission	1.3%
Total transmission	700 nJ \pm 10 nJ

vacuum windows have good transmission in the VIS to IR range as well as in the long-THz wavelength range (see Fig. 1).

Pulse energies of the XUV, measured with the gas-monitor detector (GMD), were 110 $\mu\text{J} \pm 20 \mu\text{J}$ (r.m.s.) (Tiedtke *et al.*, 2009) and 0.5 $\mu\text{J} \pm 0.1 \mu\text{J}$ (r.m.s.) for the THz beam measured with a calibrated pulse energy meter (Zapolnova *et al.*, 2018; Pan *et al.*, 2019).

The estimated XUV pulse energy through the beamline (Tiedtke *et al.*, 2009) after the refocusing mirror and through attenuation filters was 700 nJ \pm 10 nJ (refer to Table 1 for details), yielding a final intensity on the sample of $6.76 \times 10^9 \text{ W cm}^{-2}$ and $2.65 \times 10^9 \text{ W cm}^{-2}$, for the two measured XUV beam sizes (see Section 4 for details). By measuring both transmitted and reflected intensities of the THz beam and assuming that absorption in the excited Si layer is negligible, we are able to correct the pulse-to-pulse energy fluctuations of the THz beam (3.6% RMS at 100 μm , 14% RMS at 8 μm).

4. THz and XUV 2D beam profile

The THz and XUV beams were characterized by 2D profile measurements in the focal position. A pyro detector with a 100 μm pinhole was mounted on an *xy* positioner, facing the incoming THz and XUV beams at normal incidence, and was

moved through the focus of the beam with defined steps along the *z* axis. The pyro detector also showed a good response for XUV radiation, and therefore it was used for both the THz and XUV beam profile characterizations.

The results of 2D scans are presented in Fig. 3. The THz beam in focus has an ellipsoidal profile, elongated in the vertical direction, because of imperfect alignment of the off-axis parabolic mirror for the THz beam. The full width at half-maximum (FWHM) diameter of the THz beam with the THz undulator set at a 100 μm nominal wavelength was $400 \pm 20 \mu\text{m} \times 1470 \pm 30 \mu\text{m}$, and at 8 μm it was $180 \pm 15 \mu\text{m} \times 320 \pm 15 \mu\text{m}$. In an attempt to match the XUV and THz beam sizes we inserted a pinhole (3 mm diameter) in the XUV beam, 30 m upstream of the experiment, to optimize the ratio between beam sizes. The FWHM diameters of the XUV beam with and without a pinhole were $230 \pm 30 \mu\text{m}$ and $140 \pm 20 \mu\text{m}$, respectively. The ratio between the areas of the THz and XUV beams was 1:9 for the THz beam at 100 μm and 2:3 at 8 μm .

5. Transient reflectivity and transmission

Results of time-dependent reflectivity measurements [presented as $(R - R_0)/R_0$, where R_0 is the equilibrium reflectivity] are presented in Fig. 4. Once the probing THz pulse arrives following the XUV pulse, a portion of the THz pulse, which spatially overlaps with the XUV pulse, is reflected more because of the plasma created by the XUV pulse. The observed duration of the transition (slope) $\Delta\tau_{\lambda_{\text{THz}}}$ is the convolution of the pulse durations of the THz $\Delta\tau_{\text{THz}}$ and XUV pulses $\Delta\tau_{\text{XUV}}$, the jitter $\Delta\tau_{\text{jitter}}$ between them, and the timescale of the free carrier excitation process $\Delta\tau_{\text{excitation}}$, and can be described as

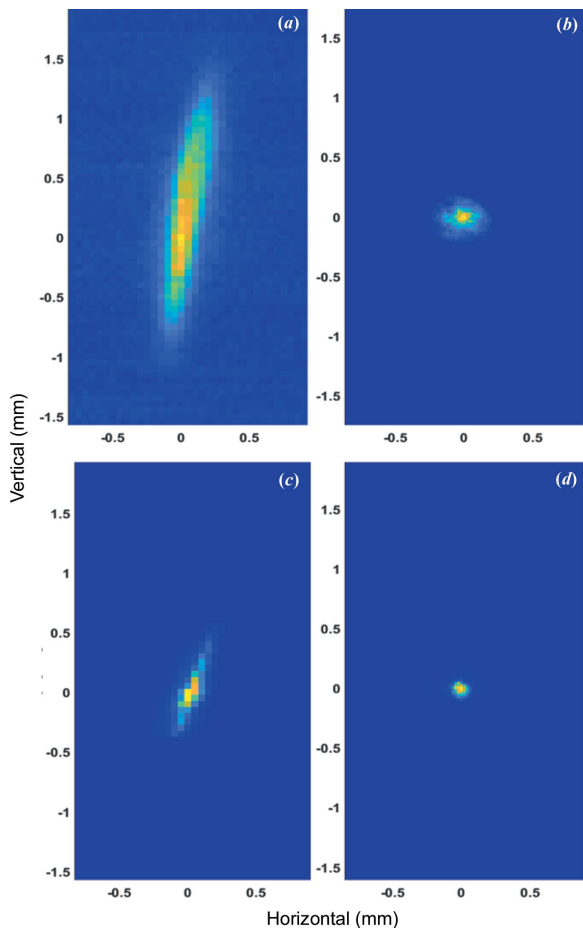


Figure 3
Measured 2D profiles of the THz and XUV beams. (a) THz beam profile at 100 μm with an FWHM of $400 \pm 20 \mu\text{m} \times 1470 \pm 30 \mu\text{m}$. (b) XUV beam at 13.5 nm wavelength through a 3 mm pinhole placed ~ 30 m upstream of the experiment with an FWHM of $230 \pm 30 \mu\text{m}$. (c) THz beam profile at 8 μm wavelength with an FWHM of $180 \pm 15 \mu\text{m} \times 320 \pm 15 \mu\text{m}$. (d) XUV beam at 13.5 nm wavelength with a 10 mm pinhole at the same position as in (b) with an FWHM of $140 \pm 20 \mu\text{m}$.

$$\Delta\tau_{\lambda_{\text{THz}}} = (\Delta\tau_{\text{THz}}^2 + \Delta\tau_{\text{XUV}}^2 + \Delta\tau_{\text{jitter}}^2 + \Delta\tau_{\text{excitation}}^2)^{1/2}.$$

For a THz wavelength of $\sim 100 \mu\text{m}$, the observed slope width is $\Delta\tau_{100\mu\text{m}} = 2.2$ ps and for 8 μm wavelength it is $\Delta\tau_{8\mu\text{m}} = 1.2$ ps (calculated as the time between the points corresponding to the 10% and 90% levels of total amplitude of the signal). The XUV and THz pulses are naturally synchronized in this experiment, with jitter smaller than 5 fs (RMS) (Frühling *et al.*, 2009), and its contribution is negligible. We assume that the excitation of the free carriers is much faster than other time-scales in the experiment so we neglect it as well.

6. Dependence on the XUV fluence

Fig. 5 shows a comparison of the transient THz reflectivity change for different fluences of the pump XUV pulse. We used different combinations of the attenuation filters: Si_3N_4 350 nm (red line), Si_2N_4 350 nm + Nb 405 nm (orange line) and Si_3N_4 500 nm (green line). The effect of the plasma switch in

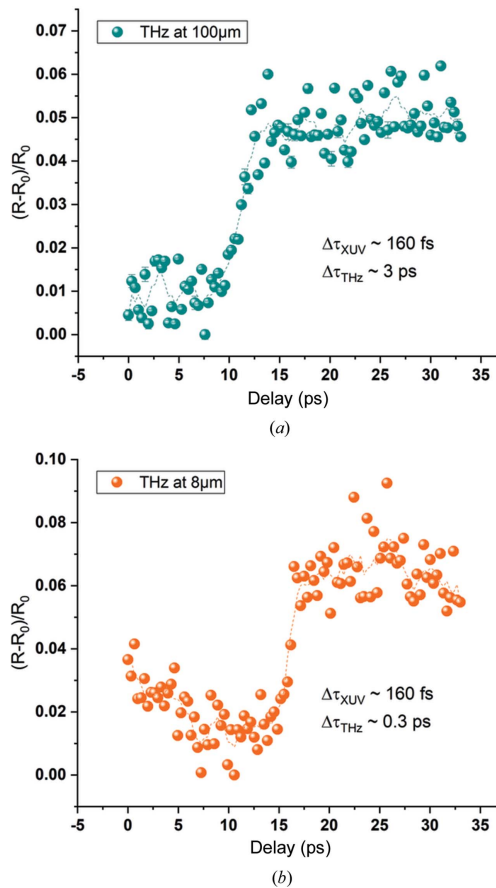


Figure 4
Transient optical reflectivity curves for the THz undulator set at 100 μm and 8 μm wavelengths for a 13.5 nm XUV pump wavelength.

the THz spectral range is very efficient and can be clearly observed even at XUV fluences as low as $45 \mu\text{J cm}^{-2}$.

7. Quantitative estimate of the effect

The amplitude of the reflectivity change for a broadband THz beam $> 100 \mu\text{m}$ is around 6.4% and for 8 μm is around 6.0%. Using the details of the actual THz and XUV beam sizes

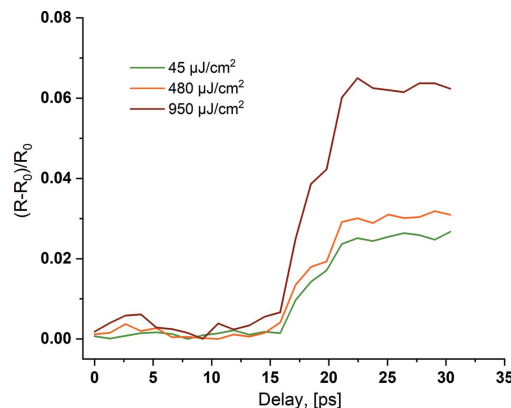


Figure 5
Transient THz reflectivity curves as a function of the THz/XUV pulse delay for three different fluences of the XUV pulse on the sample.

from the 2D profile measurements, we can estimate the actual switched fraction of the THz pulse. Comparing total areas of the beams and assuming that the electron density follows the intensity envelope of the XUV beam linearly, we can assume that, if the XUV beam size matches the size of the THz beams for a 100 μm wavelength (400 μm FWHM beam size) and for a 8 μm wavelength (180 μm FWHM beam size), the overall effect on the reflectivity change would be 9 times higher ($\sim 57.6\%$) and 1.5 times higher ($\sim 10\%$) than observed.

8. Summary

We have developed a tool for temporal and spatial overlap of XUV and THz pulses in pump–probe experiments, based on an XUV plasma switch for the THz range on an Si sample. During several pump–probe experiments at FLASH, it was demonstrated that the arrival time of XUV and THz pulses can be established down to at least the pulse duration of the THz pulse.

The experiment has been performed at different XUV fluences from 0.045 mJ cm^{-2} up to 0.95 mJ cm^{-2} for 8 μm wavelength and for the broadband $>100 \mu\text{m}$ wavelength of the probe pulse. The observed change of the transient normalized reflectivity $(R - R_0)/R_0$ of THz beam due to the plasma switch is approximately 6% from the initial level.

Since this effect uses low XUV fluences, far below the damage threshold, and uses room-temperature broadband THz detectors, it is robust and simple. This technique can be further applied at facilities employing XUV–THz pump–probe experiments, and enables a straightforward and efficient method for temporal overlap of XUV and THz pulses on the picosecond time scale.

APPENDIX A

Comparison of the excited-layer thickness with the penetration depth of THz radiation

The frequency-dependent dielectric constant, according to the simple Drude model, where damping is independent of the free electron energy, can be expressed as (Van Exter & Grischkowsky, 1990)

$$\varepsilon(\omega) = \varepsilon(\infty) - \frac{\omega_p^2}{\omega(\omega + i\Gamma)},$$

where ω_p is the plasma frequency, $\Gamma = 1/\tau_c$ is the damping frequency and τ_c is the average free-electron collision time. From the literature, we estimate the average free-electron collision time to be between 1 fs and 100 fs (Ashcroft & Mermin, 1976; Temnov *et al.*, 2006; Van Exter & Grischkowsky, 1990; Riedel *et al.*, 2013). Finally, this gives us the estimated minimum penetration depth for probing THz frequencies (2–40 THz) in XUV-excited plasma in silicon to be $\geq 2 \mu\text{m}$.

For an XUV wavelength of 13.5 nm impinging at a 45° angle of incidence, the thickness of the excited area in silicon is 400 nm, as determined by the penetration depth (Henke *et al.*,

1993). The XUV pulses from FLASH, used in this work (as presented in Fig. 5), result in free-electron densities in the range from $1.2 \times 10^{17} \text{ cm}^{-3}$ up to $2.8 \times 10^{18} \text{ cm}^{-3}$.

This leads to the conclusion that only a small fraction of the probing THz radiation ($<20\%$) is absorbed in the investigated sample excited by the XUV pulse.

Acknowledgements

NS thanks Michael Gensch from German Aerospace Center (DLR)/Technical University of Berlin for fruitful discussions.

Funding information

The authors acknowledge financial support from the German Academic Exchange Service (DAAD grant Nos. 572119839 and 53793513), Bundesministerium für Bildung und Forschung (grant No. 05K12CH4).

References

- Ashcroft, N. W. & Mermin, D. N. (1976). *Solid State Physics*. New York: Holt, Rinehart and Winston.
- Cartella, A., Bonora, S., Först, M., Cerullo, G., Cavalleri, A. & Manzoni, C. (2014). *Opt. Lett.* **39**, 1485–1488.
- Danailov, M. B., Bencivenga, F., Capotondi, F., Casolari, F., Cinquegrana, P., Demidovich, A., Giangrisostomi, E., Kiskinova, M. P., Kurdi, G., Manfreda, M., Masciovecchio, C., Mincigrucci, R., Nikolov, I. P., Pedersoli, E., Principi, E. & Sigalotti, P. (2014). *Opt. Express*, **22**, 12869–12879.
- Dell’Angela, M., Hieke, F., Malvestuto, M., Sturari, L., Bajt, S., Kozhevnikov, I. V., Ratanapreechachai, J., Caretta, A., Casarin, B., Glerean, F., Kalashnikova, A. M., Pisarev, R., Chuang, Y. D., Manzoni, G., Cilento, F., Mincigrucci, R., Simoncig, A., Principi, E., Masciovecchio, C., Raimondi, L., Mahne, N., Svetina, C., Zangrando, M., Passuello, R., Gaio, G., Prica, M., Scarcia, M., Kourousias, G., Borghes, R., Giannessi, L., Wurth, W. & Parmigiani, F. (2016). *Sci. Rep.* **6**, 1–8.
- Düsterer, S., Rehders, M., Al-Shemmary, A., Behrens, C., Brenner, G., Brovko, O., Dell’Angela, M., Drescher, M., Faatz, B., Feldhaus, J., Frühling, U., Gerasimova, N., Gerken, N., Gerth, C., Golz, T., Grebentsov, A., Hass, E., Honkavaara, K., Kocharian, V., Kurka, M., Limberg, Th., Mitzner, R., Moshhammer, M., Plönjes, E., Richter, M., Rönsch-Schulenburg, J., Rudenko, A., Schlarb, H., Schmidt, B., Senftleben, A., Schneidmiller, E. A., Siemer, B., Sorgenfrei, F., Sorokin, A. A., Stojanovic, N., Tiedtke, K., Treusch, R., Vogt, M., Wieland, M., Wurth, W., Wesch, S., Yan, M., Yurkov, M. V., Zacharias, H. & Schreiber, S. (2014). *Phys. Rev. ST Accel. Beams*, **17**, 120702.
- Exter, M. van & Grischkowsky, D. (1990). *Phys. Rev. B*, **41**, 12140–12149.
- Frühling, U., Wieland, M., Gensch, M., Gebert, T., Schütte, B., Krikunova, M., Kalms, R., Budzyn, F., Grimm, O., Rossbach, J., Plönjes, E. & Drescher, M. (2009). *Nat. Photon.* **3**, 523–528.
- Gahl, C., Azima, A., Beye, M., Deppe, M., Döbrich, K., Hasslinger, U., Hennies, F., Melnikov, A., Nagasono, M., Pietzsch, A., Wolf, M., Wurth, W. & Föhlich, A. (2008). *Nat. Photon.* **2**, 165–169.
- Harmand, M., Murphy, D., Brown, D., Cammarata, M., Döppner, T., Düsterer, S. & Toleikis, S. (2012). *J. Instrum.* **7**, P08007.
- Henke, B. L., Gullikson, E. M. & Davis, J. C. (1993). *Atom Data Nucl. Data*, **54**, 181–342.
- Krupin, O., Trigo, M., Schlotter, W. F., Beye, M., Sorgenfrei, F., Turner, J. J. & Wurth, W. (2012). *Opt. Express*, **20**, 11396–11406.
- Mayer, B., Schmidt, Ch., Bühler, J., Seletskiy, D. V., Brida, D., Pashkin, A. & Leitenstorfer, A. (2014). *New J. Phys.* **16**, 063033.

- Medvedev, N. & Rethfeld, B. (2010). *New J. Phys.* **12**, 73037.
- Mezentsev, V., Petrovic, J. S., Dubov, M., Bennion, I., Dreher, J., Schmitz, H. & Grauer, R. (2007). *Proc. SPIE*, **6459**, 64590B.
- Pan, R., Zapolnova, E., Golz, T., Krmpot, A. J., Rabasovic, M. D., Petrovic, J., Asgekar, V., Faatz, B., Tavella, F., Perucchi, A., Kovalev, S., Green, B., Geloni, G., Tanikawa, T., Yurkov, M., Schneidmiller, E., Gensch, M. & Stojanovic, N. (2019). *J. Synchrotron Rad.* **26**, 700–707.
- Pfau, B., Schaffert, S., Müller, L., Gutt, C., Al-Shemmary, A., Büttner, F., Delaunay, R., Düsterer, S., Flewett, S., Frömter, R., Geilhufe, J., Guehrs, E., Günther, C. M., Hawaldar, R., Hille, M., Jaouen, N., Kobs, A., Li, K., Mohanty, J., Redlin, H., Schlotter, W. F., Stickler, D., Treusch, R., Vodungbo, B., Kläui, M., Oepen, H. P., Lüning, J., Grübel, G. & Eisebitt, S. (2012). *Nat. Commun.* **3**, 1100.
- Riedel, R., Al-Shemmary, A., Gensch, M., Golz, T., Harmand, M., Medvedev, N., Prandolini, M. J., Sokolowski-Tinten, K., Toleikis, S., Wegner, U., Ziaja, B., Stojanovic, N. & Tavella, F. (2013). *Nat. Commun.* **4**, 1731–1737.
- Schmid, G., Schnorr, K., Augustin, S., Meister, S., Lindenblatt, H., Trost, F., Liu, Y., Stojanovic, N., Al-Shemmary, A., Golz, T., Treusch, T., Gensch, M., Kübel, M., Foucar, L., Rudenko, A., Ullrich, J., Schröter, C. D., Pfeifer, T. & Moshhammer, R. (2019). *Phys. Rev. Lett.* **122**, 073001.
- Schmidt, J., Winnerl, S., Seidel, W., Bauer, C., Gensch, M., Schneider, H. & Helm, M. (2015). *Rev. Sci. Instrum.* **86**, 063103.
- Temnov, V. V., Sokolowski-Tinten, K., Zhou, P., El-Khamhawy, A. & von der Linde, D. (2006). *Phys. Rev. Lett.* **97**, 237403.
- Tiedtke, K., Azima, A., Von Bargen, N., Bittner, L., Bonfigt, S., Düsterer, S., Faatz, B., Frühling, U., Gensch, M., Gerth, Ch., Gerassimova, N., Hahn, U., Hesse, M., Honkavaara, K., Jastrow, U., Juranic, P., Kapitzki, S., Keitel, B., Kracht, T., Kuhlman, M., Li, W. B., Martins, M., Nuñez, T., Plönjes, E., Redlin, H., Saldin, E. L., Schneidmiller, E. A., Schneider, J. R., Schreiber, S., Stojanovic, N., Tavella, F., Toleikis, S., Treusch, R., Weigelt, H., Wellhöfer, M., Wabnitz, H., Yurkov, M. V. & Feldhaus, J. (2009). *New J. Phys.* **11**, 023029.
- Wesch, S. (2012). Dissertation. DESY, Hamburg, Germany.
- Willems, F., Smeenk, C. T. L., Zhavoronkov, N., Kornilov, O., Radu, I., Schmidbauer, M., Hanke, M., von Korff Schmising, C., Vrakking, M. J. J. & Eisebitt, S. (2015). *Phys. Rev. B*, **92**, 220405.
- Zapolnova, E., Golz, T., Pan, R., Klose, K., Schreiber, S. & Stojanovic, N. (2018). *J. Synchrotron Rad.* **25**, 39–43.

Periodic three-body orbits in the Coulomb potential

Marija Šindik,¹ Ayumu Sugita,² Milovan Šuvakov,³ and V. Dmitrašinović^{3,*}

¹*Faculty of Physics, University of Belgrade, Studentski Trg 12, 11000 Belgrade, Serbia*

²*Department of Applied Physics, Osaka City University, 3-3-138 Sugimoto, Sumiyoshi-ku, Osaka 558-8585, Japan*

³*Institute of Physics Belgrade, University of Belgrade, Pregrevica 118, Zemun, 11080 Belgrade, Serbia*



(Received 30 July 2018; published 7 December 2018)

We numerically discovered around 100 distinct nonrelativistic collisionless periodic three-body orbits in the Coulomb potential *in vacuo*, with vanishing angular momentum, for equal-mass ions with equal absolute values of charges. These orbits are classified according to their symmetry and topology, and a linear relation is established between the periods, at equal energy, and the topologies of orbits. Coulombic three-body orbits can be formed in ion traps, such as the Paul, or the Penning one, where one can test the period vs topology prediction.

DOI: [10.1103/PhysRevE.98.060101](https://doi.org/10.1103/PhysRevE.98.060101)

The Newtonian three-body problem is one of the outstanding classical open questions in science. After more than 300 years of observation, only two topologically distinct types of periodic three-body systems, or orbits, have been observed in the skies [1]: (1) the so-called hierarchical systems, such as the Sun-Earth-Moon one, to which type belong more than 99% of all observed three-body systems; (2) Lagrangian three-body systems, such as Jupiter’s Trojan satellites, to which the remaining $\leq 1\%$ belong.

There has been some significant theoretical progress on the subject over the past few years: several hundred new, topologically distinct families of periodic solutions have been found by way of numerical simulations [2–16], and unexpected regularities have been observed among them [9, 13, 15, 16] relating the periods, topologies, and linear stability of orbits.

Of course, one would like to observe at least some of the new orbits and test their properties in an experiment, but such a test would be impeded by a number of obstacles: (1) only stable orbits have a chance of actually existing for a sufficiently long time to be observed; (2) stability depends on the ratio(s) of masses, and on the value of angular momentum, neither of which can be controlled in astronomical settings; (3) even if an orbit is stable in a wide range of mass ratios and angular momenta, there is no guarantee that such a system will have been formed sufficiently frequently and sufficiently close to Earth, that it may be observed by our present-day instruments.

All of the above prompted us to look for alternative three-body systems that share (at least) some of the same properties with Newtonian three-body systems. The Coulombic potential shares one basic similarity with the Newtonian gravity—its characteristic $1/r$ (homogeneous) spatial dependence—as well as several important differences: (1) the (much) larger coupling constant; (2) both attractive and repulsive nature; (3) naturally identical (quantized) electric charge(s); (4) ions with opposite charges may have masses equal to one part in a few

thousand; (5) ions have a finite probability of elastic scattering in head-on collisions; and (6) Coulombic bound states can be formed in table-top ion-trap experiments [17]. For these reasons we turn to the study of periodic three-body orbits bound by Coulombic potential. The application of only the Coulomb interaction amounts to a nonrelativistic approximation, which is good only in the low-velocity limit [18].

In this Rapid Communication we present the results of a search that led to around 100 distinct collisionless orbits, only four of which are stable, and around 80 isosceles quasicolliding (free-fall, or “brake”) ones. We use the collisionless orbits to display a new regularity, akin to Kepler’s third law, in the form of a linear dependence

$$T|E|^{3/2} \sim N, \quad (1)$$

between the scale-invariant period $T|E|^{3/2}$, where T is the period, and E is the energy of an orbit, on one hand, and the orbit’s topological complexity N , expressed as the number of collinear configurations (“syzygies”) encountered during one cycle (see the text below), on the other. This prediction ought to be tested in ion-trap experiments.

We used the same search method as in the Newtonian gravity three-body problem [5]. There are 12 independent variables that define the initial state of this system; for each body there are the x and y coordinates of the body, and the v_x and v_y components of their velocity. Adopting the center-of-mass reference frame reduces this number (12) to eight. Fixing the value of angular momentum ($L = 0$) reduces this further to six. Using the scaling rules [19] for the solutions and the fact that periodic solution must pass through at least one syzygy (collinear configuration) during one period, yields a four-dimensional search space for all zero-angular-momentum periodic solutions. We search for solutions in the two-dimensional subspace of orbits that pass through the Euler configuration, defined as the symmetric collinear configuration wherein the positively charged particle with velocity $(-2v_x, -2v_y)$ passes through the origin $(0, 0)$, i.e., exactly between the two negatively charged particles, which, in turn, pass through the points $(-1, 0)$ and $(1, 0)$, both with velocity equal to (v_x, v_y) .

*Author to whom correspondence should be addressed: dmitrasin@ipb.ac.rs

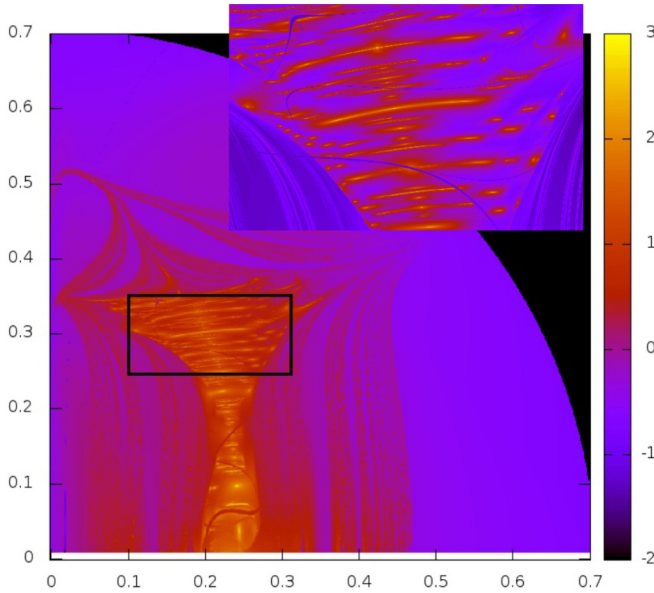


FIG. 1. Negative logarithm of return proximity function as a function of the initial velocity components v_x and v_y on the x and y axes, respectively. Bright areas correspond to high values of the negative logarithm. Inset: zoom-in of the “boxed-in” region.

In order to search for periodic solutions numerically, we have discretized the search window in this two-dimensional subspace and calculated the return proximity function (RPF) $d_{T_0}(v_x, v_y)$ that measures how close to the initial condition the trajectory returns (see [20]) up to some predefined upper limit on the integration time T_0 , at each grid point. The negative logarithm of the computed RPF is shown in Fig. 1. Local minima of RPF are used as candidates for periodic solutions. After applying the gradient descent algorithm starting at each candidate point, we have declared as periodic the solutions with RPF of $\mathcal{O}(10^{-8})$ and smaller.

We have followed the example set by three-body orbits in Newtonian gravity [5,13], and classified the newly found Coulombic orbits according to their topologies, studied their stability, and organized them into sequences some of which, although fewer in number, appear very similar to the Newtonian ones. Each orbit has a well-defined topology which can be algebraized in at least two different ways (see [20] and Refs. [21,22]). Here we use Montgomery’s method [21] wherein each solution is associated with [the conjugacy class (see [5]), of] an element of the two-generator $(a, b, A = a^{-1}, B = b^{-1})$ free group $F_2(a, b)$.

There are important distinctions among the 100-odd orbits: (1) the orbits can be separated into two classes, using their symmetry: class A consists of orbits that are symmetrical under two perpendicular reflections, and class B of orbits with a point reflection symmetry; (2) each of the classes can be further separated into sequences, defined by their free-group elements, as follows. For both class A and class B, sequence (I): $w_{n,k}^{(I)} = [(AB)^n(ab)^n]^k$ with integers $n, k = 1, 2, 3, \dots$; and for class A only, sequence (II): $w_{m,n,k}^{(A,II)} = [(AB)^m(ab)^n]^k A[(BA)^m(ba)^n]^k B$, with $m, n, k = 1, 2, 3, \dots$; and sequence (III): $w_n^{(III)} = [(ab)^2 ABA(ba)^2 BAB]^n$, with $n = 1, 2, 3, \dots$

Note that the 100-odd collisionless Coulombic orbits are substantially fewer than roughly 200 collisionless Newtonian orbits with similar search parameters, and that there are only four linearly stable solutions in contrast to more than 20 in the Newtonian case.

All of this is a consequence of just one sign change in the potential: one pair of charged particles must experience repulsion, contrary to Newtonian gravity, where all pairs are attractive. Therefore, no choreographic solution, i.e., permutationally symmetric solution with all three particles following the same trajectory, such as the famous “figure-8” orbit, may exist in the Coulombic case. Moreover, at least one orbit, similar to Orlov’s [4] colliding “S orbit” (in Newtonian gravity) still exists in the Coulombic case, but it is not stable anymore, and consequently does not produce an infinite sequence of periodic orbits (see [13]).

The initial conditions of all 100-odd orbits and their corresponding topological and kinematical properties can be found in [20]; in Fig. 2 and Table I we have shown six representative solutions.

Next we show that Eq. (1), the (striking) property of orbits that was first observed in Newtonian three-body systems [9], also features in the Coulombic three-body systems. This relation between topological and kinematical properties of Newtonian three-body systems was first reported in [9] and later studied in more detail in Refs. [11,13,15,16]. Equation (1) is a (simple) linear dependence of the scale-invariant period $T|E|^{3/2}$ on the topological complexity N . The topological complexity N can be measured in at least two different ways: (1) we used the length N_w of the free-group element (word) describing the orbit’s topology, which, due to symmetry in our case, is equal to the number of asymmetric syzygies, i.e., collinear configurations wherein the two equal-charge particles are next to each other, over one period; (2) the number N_e of *all* syzygies (collinear configurations) was considered in Refs. [9,13] as the measure of topological complexity N of Newtonian orbits.

In Fig. 3 one can see that Eq. (1) holds for three-body orbits in the Coulomb potential: (1) with $N = N_w$, a linear fit yields a slope equal to 1.8252, with asymptotic standard error of 0.08% and an average relative deviation of points from fit values that equals 0.63%; (2) with $N = N_e$ the number of *all* syzygies (collinear configurations), in the Coulomb case, the situation is slightly different (see inset in Fig. 3): the slope of this fit is 1.0208, the asymptotic standard error is 0.36%, but with a significantly larger (2.6%) average relative deviation of points from fit values.

As mentioned earlier, only four solutions are linearly stable. We solved the equations for an infinitesimal deviation from the exact periodic solution along each periodic orbit to find the eigenvalues of the monodromy matrix (see [20]). Due to the symmetry of the equations of motion, these eigenvalues appear as two ($i = 1, 2$) quadruples $(\lambda_i, \lambda_i^*, 1/\lambda_i, 1/\lambda_i^*)$. For only four orbits listed in Table II both eigenvalues λ_i have moduli equal to unity $|\lambda_i| = 1$, within their respective margins of error, which means that the corresponding three-body orbit is linearly stable.

Thus we have shown that some of the phenomena first observed in Newtonian three-body orbits, such as the linear dependence of the scale-invariant period on the topology

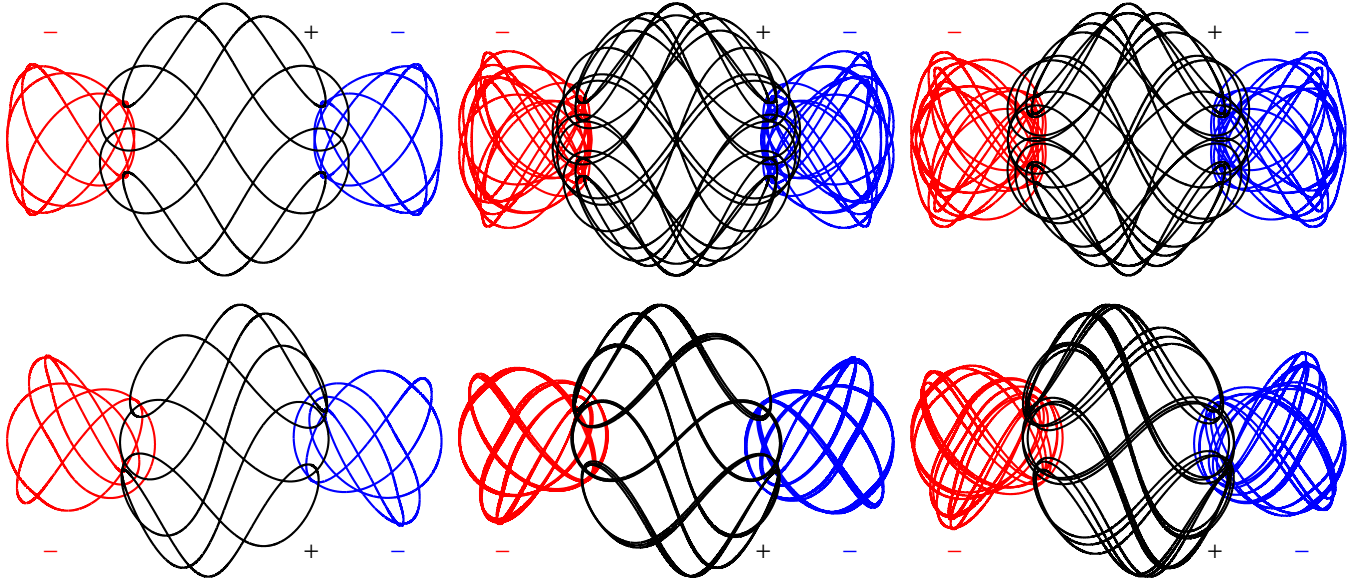


FIG. 2. Trajectories of orbits A.4, with topology $(AB)^2(ab)^2$; A.12.a and A.12.b, both with topology $[(AB)^2(ab)^2]^3$, in class A (upper row); and orbits B.4, with topology $(AB)^2(ab)^2$, and B.12.a and B.12.b, both with topology $[(AB)^2(ab)^2]^3$, in class B (lower row), respectively. Note the independent symmetries of the class A (upper row) trajectories with respect to the reflections about the horizontal and the vertical axis, whereas the class B (lower row) trajectories have only this symmetry under combined reflections. Black lines correspond to the positively charged particle while red and blue lines correspond to the negatively charged ones.

of the orbit, and the emergence of sequences [23] exist in Coulombic three-body orbits, and are not features of Newtonian gravity alone. The homogeneity [19] of the Coulombic, Newtonian, and the strong Jacobi-Poincaré potentials is common to all three known cases of manifestation of this regularity [9,13,25]. This supports indirectly the explanation offered in Refs. [13,25].

Our next concern ought to be the observation of some of these orbits in an experiment. The trajectories of a number (ranging between 1 and 32) of positively charged particles moving in a Paul trap have been photographically recorded as early as 1959 [17,26]. The challenge to actually confine and

photograph a few oppositely charged macroscopic particles in an ion trap has remained unanswered to the present day, to our knowledge. It is well known that Paul and/or Penning traps can lead to binding of pairs of identical ions, including periodic orbits as well as their chaotic motions [27,28], when the circumstances (such as the frequency and amplitudes of the applied electric and/or magnetic fields) are right. Such periodic orbits are impossible in free space, however, as there the identical ions experience only Coulomb repulsion [29]. So, before one observes any periodic three-body orbits in an ion trap, and declares them genuine Coulomb orbits, one must know which periodic three-body orbits exist in free space—

TABLE I. Initial conditions of six orbits, depicted in Fig. 2, that belong to the sequence described by the free-group elements $[(AB)^2(ab)^2]^k$, with $k = 1, 2, 3, \dots$, and four linearly stable orbits, Table II. The columns correspond to solution label, name of the sequence that the solution belongs to, initial velocities $[\dot{x}_1(0)$ and $\dot{y}_1(0)]$, period, negative energy, scaled period, free-group element, number of letters in free-group element (equal to the number of asymmetric syzygies), and the total number of syzygies over a period. For initial conditions of all other found solutions, see [20].

Label	Seq.	$\dot{x}_1(0)$	$\dot{y}_1(0)$	T	$-E$	$T E ^{3/2}$	Free-group element	N_w	N_e
A.4	I	0.191764	0.330958	13.4332	1.06108	14.6826	$(AB)^2(ab)^2$	8	14
A.12.a	I	0.147917	0.323693	37.1599	1.12003	44.0473	$[(AB)^2(ab)^2]^3$	24	42
A.12.b	I	0.246251	0.335527	45.3784	0.980345	44.0472	$[(AB)^2(ab)^2]^3$	24	42
B.4	I	0.111427	0.305087	11.3981	1.18352	14.6755	$(AB)^2(ab)^2$	8	14
B.12.a	I	0.327539	0.337033	57.4554	0.83738	44.0266	$[(AB)^2(ab)^2]^3$	24	42
B.12.b	I	0.345214	0.344247	63.0644	0.786962	44.0266	$[(AB)^2(ab)^2]^3$	24	42
A.15.b	II	0.108065	0.323579	44.7536	1.15086	55.2534	$(ab)^2ABA(ba)^2bABA$ $\times (ba)^2BAB(ab)^2aBAB$	30	52
A.18	III	0.105224	0.336995	55.6513	1.12609	66.5019	$(ab)^2ABA(ba)^2(BA)^2bab$ $\times (AB)^2aba(BA)^2(ba)^2BAB$	36	62
A.20.b	I	0.126494	0.315968	59.3293	1.15249	73.4049	$[(ab)^2(AB)^2]^5$	40	70
A.24.a	II	0.249577	0.291337	80.2223	1.0585	87.364	$[(ab)^2(AB)^2A]^2(ba)^2b$ $\times (AB)^2[(ab)^2a(BA)^2B]^2$	48	86

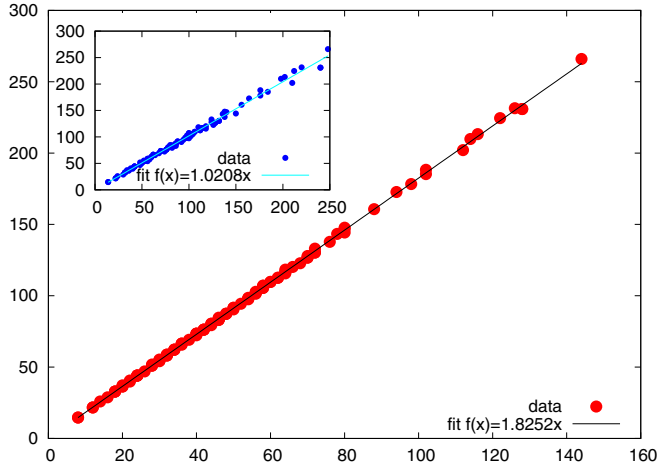


FIG. 3. Dependence of the scale-invariant period $T|E|^{3/2}$ on the number of asymmetric syzygies N_w (collinear configurations with two particles of the same charge on one side) during an orbit. Inset: dependence of the scale-invariant period $T|E|^{3/2}$ on the number of all syzygies N_e .

information that we have provided here. With the present work we have prepared the terrain for future numerical, and we hope also experimental studies of three-ion motions in traps [17].

Naturally, the orbits that are (linearly) stable in free space are also expected to exist in a trap; that is not to say that the unstable orbits cannot be stabilized by appropriate trapping fields, or that new kinds of periodic orbits cannot be formed in a trap. Moreover, ions have a nonzero elastic head-on collision cross section, unlike the stars and/or planets, so one may even observe some “colliding” orbits [31] in ion traps. This gives one an opportunity to observe hitherto experimentally unobserved orbits and to study some of their unprecedented properties.

At any rate, trap-induced corrections will have to be calculated for each three-ion orbit in any trap where experiments are conducted, before an interpretation is given. With this Rapid Communication we hope to start a discussion of trap-induced corrections for periodic three-ion orbits: in order to calculate such corrections, one needs the (initial conditions of) free-space periodic orbits, of which we have provided around 100, which ought to suffice for a starting point.

There are no records, to our knowledge, of searches for periodic Coulombic three-body systems with equal masses

TABLE II. Stability coefficients λ_j, ν_j , with $j = 1, 2$, of linearly stable (double elliptic) orbits, where $\lambda_j = \exp(2\pi i \nu_j)$.

Name	$\text{Re}(\lambda_i)$	$\text{Im}(\lambda_i)$	$ \lambda_i ^2$	ν_i	N_w
A.15.b	0.510145	0.860102	1.000023	0.164797	30
A.15.b	-0.11507	0.993357	0.999999	0.268355	30
A.18	-0.002025	0.999961	0.999926	0.250322	36
A.18	-0.820340	0.571882	1.000007	0.403107	36
A.20.b	0.009875	0.998966	0.998031	0.248427	40
A.20.b	0.94189	0.339728	1.002572	0.055094	40
A.24.a	-0.988601	0.174067	1.007631	0.472261	48
A.24.a	0.993975	0.116863	1.001643	0.018627	48

and equal charges, which are the closest to the equal-mass Newtonian system that was studied in Refs. [4–12,14–16]. As we wished to compare the closest analog of the Coulombic and Newtonian three-body systems, we had to repeat a search for periodic collisionless orbits at the present mass and charge ratios.

To be sure, we are not the first ones who have studied Coulombic periodic three-body motion: the subject has a long history (see, e.g., Refs. [32,33]), with a revival in the 1980s, since when a number of studies have been published: [34–44]. A numerical discovery of more than 8000 collinear colliding periodic orbits with He atom mass ratios was reported in Ref. [39], and of somewhat fewer collisionless ones in Ref. [40]. The initial conditions were not published, so one could not simply retrieve these previously discovered orbits and use them here.

With this Rapid Communication we also hope to induce practitioners to consider experimental searches, particularly in view of the fact that, at least in the case of past periodic-orbit discoveries, the theory did not precede experiment [17].

The work of V.D. and M. Šuvakov was supported by the Serbian Ministry of Education, Science and Technological Development under Grants No. OI 171037 and No. III 41011. M. Šindik conducted her work while she was supported by a student scholarship from the Serbian Ministry of Education, Science and Technological Development. All numerical work was done on the Zefram cluster, Laboratory for gaseous electronics, Center for Non-equilibrium Processes, at the Institute of Physics, Belgrade. We thank Marija Janković, Ana Hudomal, and Srdjan Marjanović for their help in the early stages of this work.

[1] A. Tokovinin, Dynamics of multiple stars: Observations, in *Massive Stars in Interacting Binaries*, ASP Conference Series Vol. 367, edited by N. St-Louis and A. F. J. Moffat (Astronomical Society of the Pacific, San Francisco, 2007), pp. 615–619.
 [2] C. Moore, Braids in Classical Gravity, *Phys. Rev. Lett.* **70**, 3675 (1993).
 [3] A. Chenciner and R. Montgomery, A remarkable periodic solution of the three-body problem in the case of equal masses, *Ann. Math.* **152**, 881 (2000).

[4] A. I. Martynova, V. V. Orlov, and A. V. Rubinov, *Astron. Rep.* **53**, 710 (2009).
 [5] M. Šuvakov, and V. Dmitrašinović, Three Classes of Newtonian Three-Body Planar Periodic Orbits, *Phys. Rev. Lett.* **110**, 114301 (2013).
 [6] M. Šuvakov, Numerical search for periodic solutions in the vicinity of the figure-eight orbit: Slaloming around singularities on the shape sphere, *Celest. Mech. Dyn. Astron.* **119**, 369 (2014).

- [7] M. Šuvakov, and V. Dmitrašinović, A guide to hunting periodic three-body orbits, *Am. J. Phys.* **82**, 609 (2014).
- [8] M. Šuvakov and M. Shibayama, Three topologically nontrivial choreographic motions of three bodies, *Celest. Mech. Dyn. Astron.* **124**, 155 (2016).
- [9] V. Dmitrašinović and M. Šuvakov, Topological dependence of Kepler's third law for planar periodic three-body orbits with vanishing angular momentum, *Phys. Lett. A* **379**, 1939 (2015).
- [10] P. P. Iasko and V. V. Orlov, Search for periodic orbits in the general three-body problem, *Astron. Rep.* **58**, 869 (2014).
- [11] M. R. Janković and V. Dmitrašinović, Angular Momentum and Topological Dependence of Kepler's Third Law in the Broucke-Hadjidemetriou-Hénon Family of Periodic Three-Body Orbits, *Phys. Rev. Lett.* **116**, 064301 (2016).
- [12] D. Rose, Ph.D. thesis, 'Geometric phase and periodic orbits of the equal-mass, planar three-body problem with vanishing angular momentum', University of Sydney, 2016. Available at <https://ses.library.usyd.edu.au/handle/2123/14416>
- [13] V. Dmitrašinović, A. Hudomal, M. Shibayama, and A. Sugita, Linear stability of periodic three-body orbits with zero angular momentum and topological dependence of Kepler's third law: A numerical test, *J. Phys. A: Math. Theor.* **51**, 315101 (2018),
- [14] <http://three-body.ipb.ac.rs/> and <http://three-body.ipb.ac.rs/sequences.php>
- [15] X. Li and S. Liao, More than six hundred new families of Newtonian periodic planar collisionless three-body orbits, *Sci. China, Phys. Mech. Astron.* **60**, 129511 (2017).
- [16] X. Li, Y. Jing, and S. Liao, The 1223 new periodic orbits of planar three-body problem with unequal mass and zero angular momentum, *Publ. Astron. Soc. Jpn.* **70**, psy057 (2018).
- [17] F. G. Major, V. N. Gheorghie, G. Werth, *Charged Particle Traps: Physics and Techniques of Charged Particle Field Confinement*, (Springer, Berlin/Heidelberg, 2005).
- [18] L. D. Landau and E. M. Lifshitz, *The Classical Theory of Fields*, 4th revised English ed. (Butterworth-Heinemann, Oxford, 1994).
- [19] L. D. Landau and E. M. Lifshitz, *Mechanical similarity*, in *Mechanics*, 3rd ed. (Butterworth-Heinemann, Oxford, 1976), Sec. 10.
- [20] See Supplemental Material at <http://link.aps.org/supplemental/10.1103/PhysRevE.98.060101> for periodic three-body orbits in the Coulomb potential, which includes, but is not limited to (a) tables of initial conditions, topologies of orbits; (b) figures of orbits' trajectories; (c) description of the search method; and (d) stability analysis.
- [21] R. Montgomery, The N -body problem, the braid group, and action-minimizing periodic solutions, *Nonlinearity* **11**, 363 (1998).
- [22] K. Tanikawa and S. Mikkola, Resonances, Stabilization, and Stable Chaos in Hierarchical Triple Systems, edited by V. V. Orlov and A. V. Rubinov (St Petersburg State University Press, St Petersburg, 2008), p. 26.
- [23] From a linearly stable orbit, in agreement with the Birkhoff-Lewis theorem [24].
- [24] G. D. Birkhoff and D. C. Lewis, On the periodic motions near a given periodic motion of a dynamical system, *Ann. Mat. Pura Appl.* **12**, 117 (1933).
- [25] V. Dmitrašinović, Luka V. Petrović, and M. Šuvakov, Periodic three-body orbits with vanishing angular momentum in the pairwise "strong" potential, *J. Phys. A* **50**, 435102 (2017).
- [26] R. F. Wuerker, H. Shelton, and R. V. Langmuir, Electrodynamical containment of charged particles, *J. Appl. Phys.* **30**, 342 (1959).
- [27] J. Hoffnagle, R. G. DeVoe, L. Reyna, and R. G. Brewer, Order-Chaos Transition of Two Trapped Ions, *Phys. Rev. Lett.* **61**, 255 (1988).
- [28] H. Totsuji, T. Kishimoto, C. Totsuji, and K. Tsuruta, Competition between Two Forms of Ordering in Finite Coulomb Clusters, *Phys. Rev. Lett.* **88**, 125002 (2002).
- [29] Curiously, the case of two opposite-charged, equal-mass ions had not been examined in detail, until recently (see, e.g., [30], although it also falls into the first Mathieu stability zone).
- [30] D. Trypogeorgos and C. J. Foot, Cotrapping different species in ion traps using multiple radio frequencies, *Phys. Rev. A* **94**, 023609 (2016).
- [31] We put the word colliding into quotation marks here, because only zero-angular-momentum orbits experience actual collisions, whereas ion traps generally impart (some) angular momentum to ions.
- [32] I. Langmuir, The structure of the helium atom, *Phys. Rev.* **17**, 339 (1921).
- [33] G. H. Wannier, The threshold law for single ionization of atoms or ions by electrons, *Phys. Rev.* **90**, 817 (1953).
- [34] I. Davies, A. Truman, and D. Williams, Classical periodic solutions of the equal-mass $2n$ -body problem, $2n$ -ion problem, and the n -electron atom problem, *Phys. Lett. A* **99**, 15 (1983).
- [35] H. Klar, Equilibrium Atomic Structure: Rotating Atoms, *Phys. Rev. Lett.* **57**, 66 (1986).
- [36] M. Poirier, Possible rigid rotations in two-electron atoms, *Phys. Rev. A* **40**, 3498 (1989).
- [37] P. Grujić and N. Simonović, The classical helium atom—An asynchronous-mode model, *J. Phys. B* **24**, 5055 (1991).
- [38] K. Richter and D. Wintgen, Stable Planetary Atom Configurations, *Phys. Rev. Lett.* **65**, 1965 (1990).
- [39] K. Richter, G. Tanner, and D. Wintgen, Classical mechanics of two-electron atoms, *Phys. Rev. A* **48**, 4182 (1993).
- [40] T. Yamamoto and K. Kaneko, Helium Atom as a Classical Three-Body Problem, *Phys. Rev. Lett.* **70**, 1928 (1993).
- [41] A. Santander, J. Mahecha, and F. Pérez, Rigid-rotator and fixed-shape solutions to the Coulomb three-body problem, *Few-Body Syst.* **22**, 37 (1997).
- [42] T. J. Stuchi, A. C. B. Antunes, and M. A. Andreu, Muonic helium atom as a classical three-body problem, *Phys. Rev. E* **62**, 7831 (2000).
- [43] M. M. Sano, The classical Coulomb three-body problem in the collinear eZe configuration, *J. Phys. A* **37**, 803 (2004).
- [44] F. Rupp and J. Scheurle, Genuine equilibria of three body Coulomb configurations, *Few-Body Syst.* **48**, 1 (2010).